IS-T 1689

Theoretical Study of the Noble Metals on Semiconductor Surfaces and Ti-base Shape Memory Alloys

by

Ding, Yungui

PHD Thesis submitted to Iowa State University

Ames Laboratory, U.S. DOE

Iowa State University

Ames, Iowa 50011

Date Transmitted: July 27, 1994

PREPARED FOR THE U.S. DEPARTMENT OF ENERGY

UNDER CONTRACT NO. W-7405-Eng-82.

DISCLAIMER

DISCLAIMER

Portions of this document may be illegible in electronic image products. Images are produced from the best available original document.

Theoretical study of the noble metals on semiconductor surfaces and Ti-base shape memory alloys

Yungui Ding

Under the supervision of Kai-Ming Ho
From the Department of Physics and Astronomy
Iowa State University

The electronic and structural properties of the $(\sqrt{3} \times \sqrt{3})$ $R30^\circ$ Ag/Si(111) and $(\sqrt{3} \times \sqrt{3})$ $R30^\circ$ Au/Si(111) surfaces are investigated using first principles total energy calculations. We have tested almost all experimentally proposed structural models for both surfaces and found the energetically most favorable model for each of them. The lowest energy model structure of the $(\sqrt{3} \times \sqrt{3})$ $R30^\circ$ Ag/Si(111) surface consists of a top layer of Ag atoms arranged as "honeycomb-chained-trimers" lying above a distorted "missing top layer" Si(111) substrate. The coverage of Ag is 1 monolayer (ML). We find that the honeycomb structure observed in STM images arise from the electronic charge densities of an empty surface band near the Fermi level. The electronic density of states of this model gives a "pseudo-gap" around the Fermi level, which is consistent with experimental results. The lowest energy model for the $(\sqrt{3} \times \sqrt{3})$ $R30^\circ$ Au/Si(111) surface is a conjugate honeycomb-chained-trimer (CHCT-1) configuration which consists of a top layer of trimers formed by 1 ML Au atoms lying above a "missing top layer" Si(111) substrate with a honeycomb-chained-trimer structure for its first layer. The structures of Au and Ag are in fact quite similar and belong to the same class of structural models. However, small variation in the structural details gives rise to quite different observed STM images, as revealed

in the theoretical calculations. The electronic charge density from bands around the Fermi level for the $(\sqrt{3} \times \sqrt{3})$ $R30^\circ$ Au/Si(111) surface also gives a good description of the images observed in STM experiments.

First principles calculations are performed to study the electronic and structural properties of a series of Ti-base binary alloys TiFe, TiNi, TiPd, TiMo, and TiAu in the B2 structure. Calculations are also done for Ti in bcc structure and hypothetical B2-structured TiAl, TiAg, and TiCu. Our results show corelation between the Martensitic transformation temperature (M_s) of these alloys and the electronic properties such as the total electronic density of states at the Fermi level, occupation of the Ti d states, and the degree of localization of the d states of the second element in the alloys. Angular momentum decomposition of the electronic states indicates that the bonding of d electrons of the two elements plays an important role in the stability of the binary alloys. Correlations between M_s and optimized structural parameters such as lattice constants and bulk moduli are also found.

Theoretical study of the noble metals on semiconductor surfaces and Ti-base shape memory alloys

by

Yungui Ding

A Dissertation Submitted to the

Graduate Faculty in Partial Fulfillment of the

Requirements for the Degree of

DOCTOR OF PHILOSOPHY

Department: Physics and Astronomy
Major: Condensed Matter Physics

Approved:

In Charge of Major Work

For the Major Department

For the Graduate College

Iowa State University
Ames, Iowa
1993

TABLE OF CONTENTS

LIST OF TABLES

LIST OF FIGURES

ACKNOWLEDGEMENTS

I am very grateful to my advisor Prof. Kai-Ming Ho, and to Dr. Che-Ting Chan for their guidance and support during this research. Their kindness, enthusiasm, knowledge, and encouragement have made my graduate study at Iowa State University very enjoyable. I thank Prof. Bruce Harmon, Prof. Costas Soukoulis, and Prof. Yi-ying Ye for their guidance and willingness to share their time and knowledge with me. My special thank goes to Dr. Noboru Takeuchi, who helped me in the initial stage of this work.

I would like to thank the members of my Program of Study Committee for their advice and guidance.

I thank my wife, Jianying Peng, my daughter, Julia, my parents, my parents-in-law, and all other members in my family for their everlasting support and concerns all these years.

This work was performed at Ames Laboratory under contract no. W-7405-eng-82 with the U. S. Department of Energy. The United States government has assigned the DOE Report number IS-T 1689 to this thesis. The work was supported by the National Science Foundation (Grant No. DMR-8819379), and in part by the Director for Energy Research, Office of Basic Energy Sciences, including a grant of computer time on the Cray computers at Lawrence Livermore Laboratory.

CHAPTER 1. INTRODUCTION

The behavior of noble metal overlayers on semiconductor surfaces has been a topic of great technical and fundamental interest for many years [1]. Technological importance of these systems comes from the potential applications of the Au/Si and Ag/Si interfaces in semiconductor devices. Fundamental interest arises because a wide variety of coverage-dependent structural arrangements occur, including ordered metal overlayers on reconstructed semiconductor surfaces, the formation of surface alloys, and the alteration of semiconductor reconstructions by trace amounts of metallic adsorbate. These interfacial rearrangements pose challenging problems for surface science, causing the application of many experimental and theoretical techniques to the determination of atomic positions, the nature of metal-semiconductor bonding, and the electronic structure of the interfaces.

The Ag on Si(111) surface system has been regarded as a prototypical metal/semiconductor interface partly because there is limited reaction or intermixing between the two species. Ag growth proceeds in a layer-by-layer-like fashion at room temperature with the overlayer showing features characteristic of bulk Ag after a few monolayers (ML) (see ref. [1] and references therein). Above 200°C, the growth process turns to a Stranski-Krastanov mode: at approximately one monolayer, the surface structure is characterized by a $(\sqrt{3} \times \sqrt{3})\ R30^\circ$ ($\sqrt{3}$ for short) periodicity

and further deposition results in the nucleation of three dimensional (3D) Ag crystallites. In the submonolayer region, the $\sqrt{3}$ phase undergoes a transformation to a 3×1 structure when the surface is annealed at temperatures high enough to induce some desorption of Ag. This 3×1 structure converts to a 6×1 structure upon cooling to room temperature. The atomic arrangements for each of these structures have not been totally solved.

The $(\sqrt{3} \times \sqrt{3})$ $R30^\circ$ Ag/Si(111) surface ($\sqrt{3}$-Ag, for short), in particular, is probably one of the most heavily studied metal on semiconductor system in the history of surface science [1-44]. Since the first study on this surface was reported more than twenty years ago [2], almost all surface sensitive experimental techniques have been applied to study the structure of this system and a number of conflicting structural models have been proposed [1-44]. However, although this surface can be prepared relatively easily in a reproducible manner, experimentalists have, for a long time, failed to reach a consensus on its atomic structure and other physical properties of these systems. Even the basic properties such as whether the Ag coverage is 2/3 or 1 ML and whether the Ag atoms form the topmost layer or are embedded below a Si layer have been controversial.

For the $(\sqrt{3} \times \sqrt{3})$ $R30^\circ$ Au/Si(111) surface ($\sqrt{3}$-Au), although there are not as many experiments performed on it as compared with the $\sqrt{3}$-Ag surface, the situation is no less confusing [45-61]. Experimental techniques of impact-collision ion scattering spectroscopy (ICISS) [45, 46], medium-energy ion scattering (MEIS) [47], scanning tunneling microscopy (STM) [49-52], X-ray diffraction (XRD) [53], Auger electron spectroscopy (AES) [54], angle-resolved photoelectron spectroscopy [55], LEED [56-59], and electron microscopy [60, 61] have been used for this surface.

Just from various ion-scattering experiments, different models have been proposed, which include the modified triplet coplanar model (MTC) [45], the simple honeycomb with centered hexagons (HCH) model [46], and the missing top layer twisted trimer models (MTLTT) [47]. All these experimentally proposed models for the $\sqrt{3}$-Au surface have a nominal Au coverage of 1 ML [45, 47] (or close to 1 ML, as in the HCH model [46]).

Due to the complexity of the reconstruction and the wild variations in the experimental interpretations, theoretical investigation of this problem is quite difficult [63-69]. Empirical techniques are not accurate enough to provide definitive answers, and first-principles calculations, even with the state-of-the-art supercomputers, are still very computer time-consuming. Nevertheless, we will summarize in this thesis our effort to study the structures of these systems via first principles calculations and show that many key issues can be settled with careful theoretical calculations.

Early calculations of the electronic structure of bulk crystals became available in the 1960s. The pseudopotential [70] approach allowed a determination of the energy band spectrum for dozens of solids. Within these early models [71], surface would be treated as the end of perfect solid, no reconstructions, surface states, or redistribution of the electronic charge were possible. To allow for charge distribution and surface reconstruction, two principal methods were developed. In one approach [72], a matching of decaying orbitals to the propagating bulk electronic wavefunctions allowed for a description of surface states and charge redistribution, which is a direct solution to the breaking of the translational symmetry caused by the surface. The second approach [73], involved the use of supercells [74] to accommodate localized geometries. An artificial supercell models a surface by assuming a slab geometry

containing certain layers of Si atoms with a vacuum region on both sides. The slabs are repeated infinitely, and the top and bottom layers of the slab are associated with the solid surfaces. A self-consistent calculation of the electronic states is performed [72-74]. This approach could help to understand the electronic structure of surfaces and the consequences of surface reconstruction for electronic behavior.

Bulk structural calculations improved dramatically around 1980. By using *ab initio* pseudopotential [75-80] and a momentum space formalism [81], it became possible to calculate the total energy for different arrangements of atoms to find the lowest energy structure [82]. The extension of total energy techniques designed for bulk properties to surfaces came through the use of supercells [83-85].

Today's advancement and development of computer technology is allowing the study of newer systems using modern band theoretical methods. At present, the most satisfactory approach to the description of electron-electron interaction in crystals is based on the local-density-functional (LDF) formalism [102]. The central quantity of LDF is the total energy, which is a variational minimum of the real ground state charge density. By accurately evaluating the ground state total energy self-consistently as a function of atomic position, we can determine surface geometries. For a surface, the energy is computed as the geometry is changed, and the minimum energy configuration is the local minimum energy structure. Related to this approach is the calculation of the Hellmann-Feynman forces on the surface atoms [103]. With the density fixed with a starting geometry, the forces on each surface atom in the slab supercell are computed, and the atoms are moved then in the direction of the forces. The procedure is repeated with the new geometry until the forces are zero. The force calculation helps to find the minimum energy structure quickly. Many

surface geometries have been accurately determined by using this approach [86-101]. In this thesis, we study the complex reconstruction of Ag and Au on Si(111) surface using first-principles total energy calculations. These calculations also allow us to investigate the microscopic electronic causes of these geometries. We also use local-density-functional theory to explain the physical causes of the reconstruction of Ag and Au on Si(111).

Throughout our calculations, we use the frozen core approximation. In this approximation, the nuclei plus the core electrons are considered as rigid ions which are assumed to be unresponsive to the change in their chemical environment. Since the electronic properties of crystalline solids are most of the times dictated by the outermost electrons, we do not have to consider the inner electrons. The interaction of the cores and the valence electrons is then simulated by angular-momentum-dependent (non-local) pseudopotentials, which are generated using the "Norm Conserving" scheme [77]. In the pseudopotential approach, the core states are eliminated from the problem. Unlike the all electron wave-functions, the pseudo-wave-functions are smooth with no radial nodes.

The localized character of the d electrons in Ag and Au makes the expansion for the wave-function in plane waves uneconomical. We use an energy independent mixed-basis set containing plane waves and Bloch sums of localized orbitals to represent the electronic wave-function. To facilitate the calculation of the total energy, a momentum space representation is used [81]. To accelerate the convergence of the self-consistent loop, we use a dielectric matrix scheme to calculate the new input potential that drastically reduces the number of iterations [104]. In our slab calculations, the interatomic distances are fully relaxed with the help of Hellmann-Feynman

forces [105].

Ti-base binary alloys belong to a class of metallic alloys exhibiting the shape-memory (SM) effect. Most of these alloys undergo Martensitic transformations (MT) when their structural phase changes from CsCl (B2) to monoclinic primitive (B19) or other structures. The nature of such a transformation is of great interest by itself due to its promising rich physics. On the other hand, the study of such phase transitions is of great technological interest as a group of promising materials for high temperature applications due to their low density, high melting temperature with strength retention at elevated temperatures, excellent thermal conductivity, and good oxidation resistance. The physical properties of these materials such as electrical resistivity, magnetic susceptibility, internal friction, specific heat, linear expansion and optical properties have been extensively studied [106, 107]. However, a microscopic theory of the SM effect is still elusive. Recently, there are experimental data suggesting empirical relations between the transformation temperatures (M_s) and fundamental parameters of electronic and crystal structures of the alloys [106]. In this thesis, we perform first principles calculations to study the electronic and structural properties of a series of Ti-base binary alloys TiFe, TiNi, TiPd, TiMo, TiCu, TiAg, TiAu, and TiAl alloys in their B2 structure. Results show correlation between the MT temperature of these alloys and the electronic properties of the alloys.

The properties of the *ab initio* pseudopotentials used in our calculations are described in Chapter 2.

In Chapter 3, the formulation for the first-principles total energy calculations in solids, using a momentum-space formalism, is reviewed. A brief description of the mixed basis approach for the expansion of the electronic wave-function, and the

self-consistent loop are given. In this chapter, we also review briefly the Hellmann-Feynman theorem.

In Chapter 4, we study the $(\sqrt{3} \times \sqrt{3})$ $R30^\circ$ Ag/Si(111) surface using first-principles calculations. Various feasible structural models are investigated, and we find that the Honeycomb-Chain-Trimer model (HCT-1) is the energetically most favorable structural model for this surface system. The Ag coverage for this model is 1 ML. The electronic properties of selected models are carefully examined. The HCT-1 model is the only one that gives a pseudo-gap in the electronic density of states. This model can also explain the experimental STM image of the $(\sqrt{3} \times \sqrt{3})$ $R30^\circ$ Ag/Si(111) surface. Surface band structures of HCT-1 model are studied. Surface bands around the Fermi level are found to be contributing to the honeycomb structure of the STM image.

In Chapter 5, the structure of the $(\sqrt{3} \times \sqrt{3})$ $R30^\circ$ Au/Si(111) surface is investigated using first principles total energy calculations. Most models proposed by experiments have been tested. The lowest energy model is a conjugate honeycomb-chained-trimer (CHCT-1) configuration which consists of a top layer of trimers formed by Au atoms lying above a "missing top layer" Si(111) substrate with a honeycomb-chained-trimer structure for its first layer. The electronic charge densities from bands around the Fermi level gives a good description of the images observed in STM experiments.

In Chapter 6, we study the electronic and structural properties of a series of Ti-based binary alloys TiFe, TiNi, TiPd, TiMo and TiAu in the B2 structure by using first principles calculations. Calculations are also done for Ti in bcc structure and hypothetical B2-structured TiAl, TiAg and TiCu. Results show corelation between

the Martensitic transformation temperatures (M_s) and the electronic properties of these alloys.

CHAPTER 2. NORM-CONSERVING PSEUDOPOTENTIALS

Introduction

A solid state system is a congregation of atoms, which is a many particle system of atomic nuclei and electrons. To study the properties of any such system is to solve a complicated Schrödinger (or Dirac) equation. Due to the large mass difference between the nuclei and electrons, the many-body system can be approximated by assuming that the electrons are adiabatically following the nuclei and are always in their ground state with respect to the actual nuclear configuration. That is well known as the Born-Oppenheimer approximation, in which the motions of the nuclei and the electrons can be considered separately. That leaves us with a many electron system subject to the Coulomb potential from the nuclei in many studies of solid state physics.

However, it is still too difficult a problem to tackle without further simplifications. It is still impossible to calculate the wavefunction for all the electrons in a solid even with today's computer capabilities, therefore we have to pick out the essential factors that describe the problem and drop out other minor effects, as long as that does not affect the solution in a significant way. We find that a solid can also be thought of as a set of rather tightly bound spherical ions (the atomic cores) sitting in the electron cloud formed by the valence electrons. These valence electrons are

responsible for almost all the ordinary physical and chemical properties. The idea of pseudopotential was then introduced to simplify electronic structure calculations by eliminating the atomic core states and the strong potentials responsible for binding them [108].

The concept of pseudopotentials has developed over a few decades. At the beginning, two distinct lines of development were discernible: in one, ion pseudopotentials of enforced smoothness were empirically fitted to reproduce experimental energy bands [109]. Consequently, wave-functions were only approximately described. The second one has its origin in the Orthogonalized-Plane-Wave (OPW) method for band structure calculations introduced by Herring [110]. For the wavefunctions of the electrons in the crystal he used a linear combination of core states and plane waves that he made orthogonal to the filled core states. This approach produces wave-functions that are plane wave-like except in the core region where they must have enough oscillations in order to be orthogonal to the core-state wave-functions. In the late '50s, Phillips and Kleinman [111] showed that Herring's wave-functions can be derived as solutions for a problem in which a repulsive potential cancels much of the core potential, producing a net weak pseudopotential. These pseudopotentials are generally strongly repulsive at the origin, making it difficult to employ Fourier analysis in solids because of the large number of basis functions required. The resulting wave-functions generally exhibit the correct shape outside the core region; however they differ from the real wave-functions by a normalization factor.

Computationally, pseudopotentials are easier to deal with since the charge density from a pseudopotential is less sharp than that from the full potential. For this reason, empirical pseudopotential method was further developed where the pseudopo-

tential is usually fitted to atomic data [70]. After a process of refining the concept of pseudopotential, the modern pseudopotentials are generated such that they exactly reproduce the all-electron valence orbital outside some core radius. There are usually additional conditions imposed, such as norm-conservation [77] and the smoothness of the potential [78, 126]. Recent efforts are being made in developing softer and more transferable pseudopotentials [127-129]. In our studies, norm-conserving pseudopotentials are used.

Concept of Norm-conserving Pseudopotentials

Since the pseudopotential is a device to eliminate the core states from the problem, the pseudo-wave-functions need only to reproduce the true valence wave-functions in the valence region. There is no need to refer to the core states and the pseudo-wave-functions do not need to be orthogonal to the core-state wavefunctions. This is the idea of the "Norm-Conserving" pseudopotential developed by Hamann, Schlüter, and Chiang [112]. Their new family of energy-independent pseudopotentials have the following properties:

1. The pseudopotential must reproduce the corresponding eigenvalues from an all-electron calculation.

2. The pseudo-wave-function, after normalization, must be identical to the true valence wave-function outside a chosen "core radius" r_c

3. The integrals from 0 to r of the real and pseudo charge density agree for $r > r_c$ for each valence state (norm conservation)

$$\int_0^r \rho_{ps}(\mathbf{r})\mathbf{dr} = \int_0^r \rho_{el}(\mathbf{r})\mathbf{dr}, r \geq r_c, \tag{2.1}$$

4. The logarithmic derivatives of the real and pseudo-wave-function and their first energy derivatives agree for $r > r_c$.

Properties (3) and (4) are crucial for the pseudopotential to have optimum transferability among a variety of environments in self-consistent calculations in which the pseudo charge density is treated as a real physical object. Property (3) guarantees, through Gauss's theorem, that the electrostatic potential produced outside r_c is identical for the real and pseudo charge distributions.

The pseudopotential obtained in this way converges identically to the atomic Coulomb potential outside the core region for each valence state. In general, pseudopotentials are not unique and are non-local operators.

Fitting Procedure for Norm-conserving Pseudopotential

The generation of our pseudopotentials is done according to the scheme of Hamann, Schlüter, and Chiang [112]. They freed the construction of the atomic pseudo-orbital from reliance on core states. The construction proceeds as follows:

1. We first choose an appropriate atomic reference configuration, which often differs somewhat from the ground state, and carry out an *ab initio* self-consistent all electron calculation using a Herman-Skillman-like program [113]. The local-density-function approximation is used, and for the exchange correlation potential we use the Wigner [116] or Hedin-Lundqvist [114] form. We retain both the potential $V(r)$ and also $u_l(r)$, defined as r times the valence wavefunction with angular momentum l.

2. For each valence state l, we obtain the potential in the form:

$$V_{1,l}(r) = V(r)[1 - f(r/r_{cl})] + c_l f(r/r_{cl}), \tag{2.2}$$

where r_{cl} is the cutoff radius for each l. The restrictions are that $f(x)$ is a smooth "cutoff function" which approaches 0 as $x \to \infty$, approaches 1 at least as fast as x^3 as $x \to 0$, and cuts off for $x \sim 1$. The constant c_l is adjusted so that the nodeless solution w_{1l} of the radial Schrödinger equation with V_{1l} has energy ϵ_{1l} equal to the original eigenvalue ϵ_l. This potential converges to $V(r)$ for $r > r_{cl}$.

Property (1) of the last section is now satisfied, and the normalized function w_{1l} satisfies property (2) within a multiplicative constant,

$$w_{1l}(r) = \gamma_l u_l(r), \quad for\, r > r_c \tag{2.3}$$

3. Now we have to satisfy the norm-conserving constraint (conditions 2-4). We modify the intermediate pseudo-wave-function w_{1l} to

$$w_{2l}(r) = \gamma_l[w_{1l}(r) + \delta_l g_l(r/r_{cl})], \tag{2.4}$$

where $g_l(x)$ cuts off to zero for $x > 1$, and behaves as x^{l+1} at small x. The chosen asymptotic behavior of $f(x)$, and $g(x)$ guarantees the potential to be finite at the origin. The choice of cutoff functions used by Hamann, Schlüter, and Chiang is $f(x) = exp(-x^c)$, and $g_l(x) = x^{l+1}exp(-x^c)$ where c is varied in the fitting to assure the pseudo-wave-function $w_{2l}(r)$ is a smooth function. The δ_l is determined by the smaller solution of the quadratic equation resulting from the normalization requirement of the wave-function:

$$\gamma_l^2 \int_0^\infty [w_{1l}(r) + \delta_l g_l(r/r_{cl})]^2 dr = 1 \tag{2.5}$$

4. The final screened pseudopotential V_{2l} defined as that potential which produces the nodeless pseudo-orbital w_{2l} with eigenvalue $\epsilon_{2l} = \epsilon_k$, is found by inverting the radial Schrödinger equation. The result is given by:

$$\begin{aligned} V_{2l}(r) &= V_{1l}(r) + [\frac{1}{w_{2l}(r)}\frac{d^2}{dr^2}w_{2l}(r) - \frac{1}{w_{1l}(r)}\frac{d^2}{dr^2}w_{1l}(r) \\ &= \frac{\delta_l g_l(r/r_c)}{w_{1l}(r) + \delta_l g_l(r/r_c)}[\epsilon_l - V_{1l}(r) - \frac{l(l+1)}{r^2} \\ &\quad + \frac{1}{g_l(r/r_c)}\frac{d^2 g_l(r/r_c)}{dr^2}] + V_{1l}(r). \end{aligned} \tag{2.6}$$

5. The final step is to obtain the ionic pseudopotential $V_{ps,l(r)}$ by unscreening $V_{2l}(r)$:

$$V_{ps,l}(r) = V_{2l}(r) - (V_H(r) + V_{xc}(r)), \tag{2.7}$$

where $V_H(r)$ and $V_{xc}(r)$ are the Hartree and the exchange-correlation potential, respectively, which can be calculated from the pseudo charge distribution.

Applications to Zr

We have used in our calculations non-local ionic pseudopotentials generated using the norm-conserving scheme of Hamann, Schlüter, and Chiang. These angular-momentum-dependent pseudopotentials are constructed by constraining their pseudo-wave-functions to match the ground-state, all-electron, valence-electron wave-functions exactly outside some "core-radius," as well as reproducing the same atomic eigenvalues for the valence states. The resulted pseudopotentials and pseudo-wavefunctions for Zr are shown in Figures 2.1 and 2.2.

The relativistic Dirac equation [130] for the Zr atom is solved for the all-electron atomic eigenvalues, wavefunctions, and the total energies. Atomic configurations with

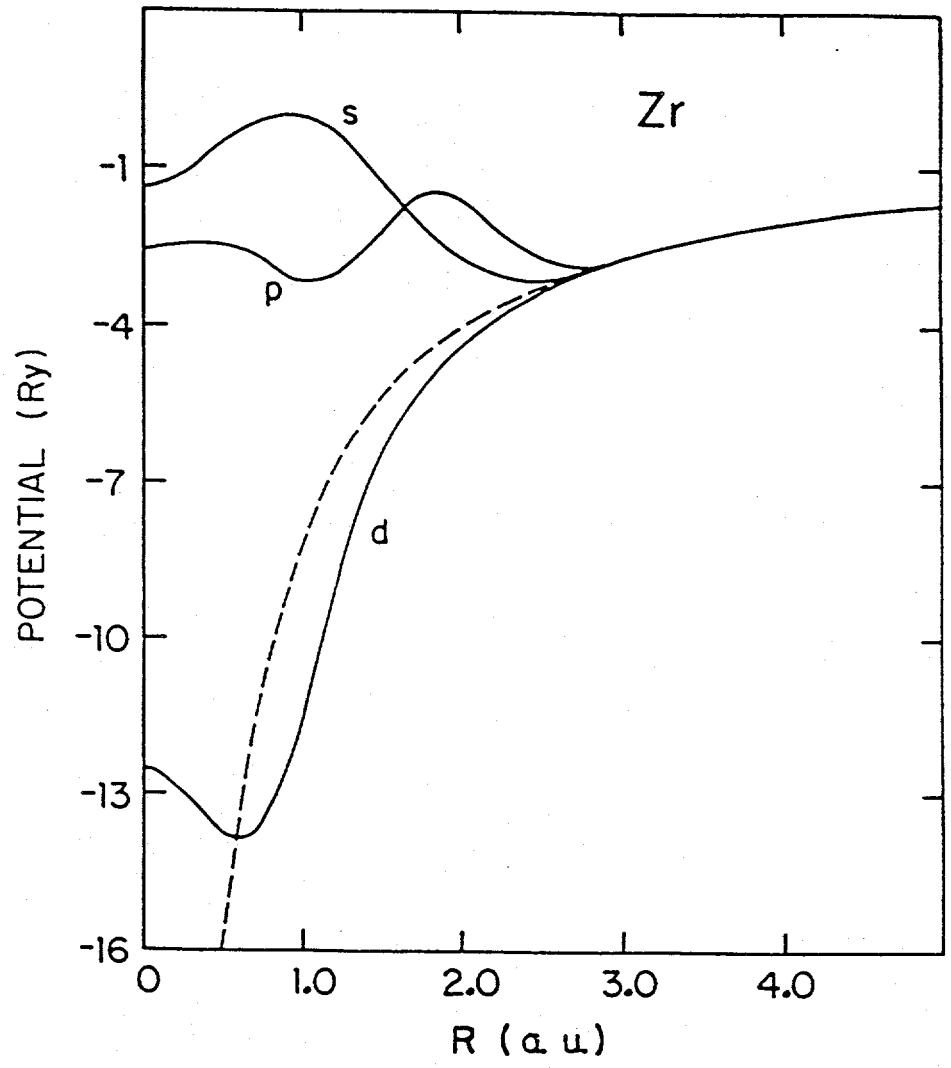

Figure 2.1: The angular-momentum-dependent pseudopotentials for Zr

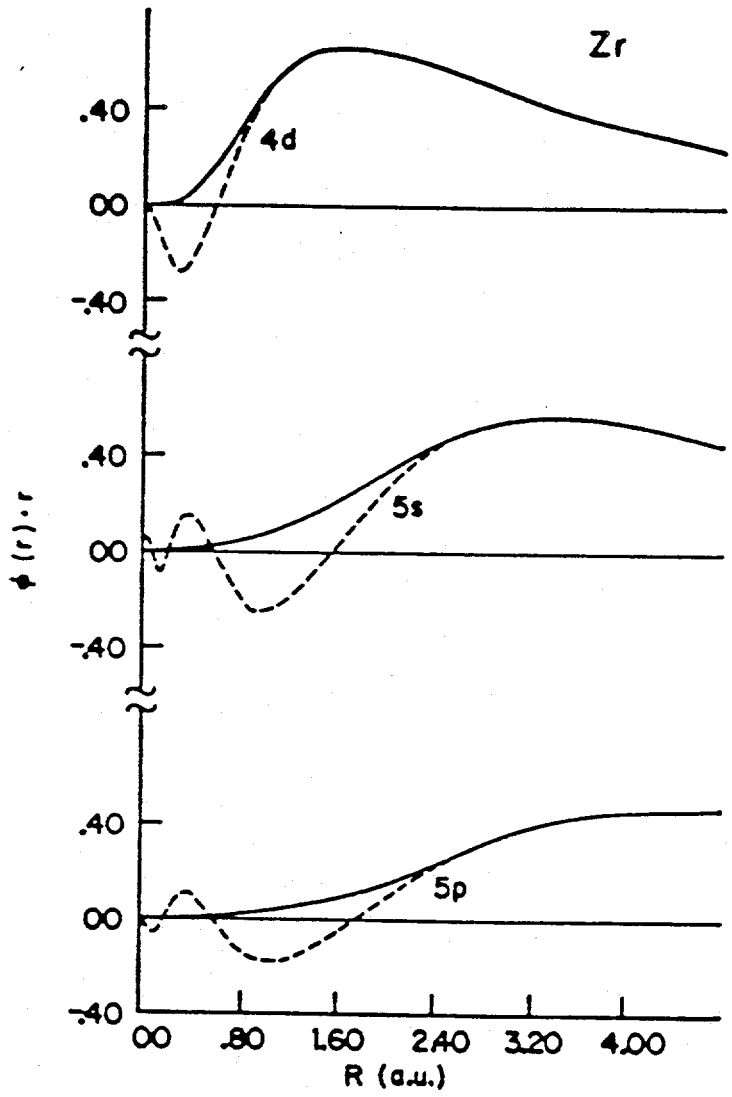

Figure 2.2: Comparison of the pseudowavefunctions (solid lines) and the corresponding all-electron valence wavefunctions for the ground state configuration of Zr

excitation energies less than 1 Ry are calculated. Since the 4p electrons are located farther away from the nucleus, they are sensitive to the configuration of the atom. Thus they are treated as valence electrons to achieve good core-valence separation and to improve the transferability of the pseudopotential to different surroundings. Compared with the partial core correction scheme [131], this approach is simpler and more straightforward in its physical concept.

To check the transferability of our pseudopotential, we compare the eigenvalues and excitation energies for various atomic configurations above the ground state obtained from the pseudopotentials with the corresponding all-electron values. The results are listed in Tables 2.1. We see that the pseudopotential results reproduced the all-electron results with an error of less than 0.008 Ry for all excited configurations.

Table 2.1: Eigenvalues and excitation energies of the pseudoatom for different configurations of Zr. Values in parentheses are results from corresponding all-electron self-consistent calculation

	Eigenvaulues (Ry)			Excitation energy (Ry)
Configuration	d	s	p	(ΔE_{tot})
$4d^2 5s^2$	-0.2830 (-0.2806)	-0.3423 (-0.3440)	-0.1220 (-0.1197)	0.0
$4d^3 5s^1$	-0.1887 (-0.1888)	-0.3027 (-0.3028)	-0.1005 (-0.0991)	0.0887 (0.0902)
$4d^4 5s^0$	-0.1306 (-0.1307)	-0.2784 (-0.2764)	-0.0903 (-0.0888)	0.2221 (0.2213)
$4d^2 5s^1 5p^1$	-0.3562 (-0.3585)	-0.3954 (-0.3984)	-0.1644 (-0.1631)	0.2270 (0.2295)
$4d^3 5p^1$	-0.2591 (-0.2619)	-0.3565 (-0.3567)	-0.1442 (-0.1433)	0.2989 (0.2983)

CHAPTER 3. GENERAL FORMALISM FOR TOTAL ENERGY IN SOLIDS

Local Density Functional Theory

To simplify the complicated many-particle solid state system, we have introduced the Born-Oppenheimer approximation and the pseudopotentials in the previous chapter. We now have a many-electron (valence electrons only) system with the pseudopotentials from the atomic cores. This system can be further reduced to a one-electron problem where the pseudopotentials the many-body interactions among electrons are represented by an effective single-electron potential. Many schemes have been developed over the years, such as the Hartree approximation, the Hartree-Fock approximation, and the local density approximation (LDA) in the density functional (DF) formalism [102], among which the LDA approach has been particularly successful, hence most widely used, in the study of ground state properties of solid state systems [115]. The electronic and structural properties of the surfaces and Ti-base alloys considered in this thesis are calculated with the density functional formalism.

Hohenberg and Kohn showed that the ground state total energy of a many-electron system in the presence of an applied external potential (in our case, the valence electrons in the presence of the ionic potentials) is a unique functional of the charge density $\rho(\mathbf{r})$, and this functional has its minimum value at the correct charge

density $\rho(\mathbf{r})$ with respect to variation of the charge density subject to the constraint of electron number conservation (known as the Hohenberg-Kohn theorem). Unlike the Hartree-Fock type approximation, the basic variable in the DF approach is the electron density in stead of the electron wavefunction. In this approach, the total energy can be expressed in atomic units (a.u.) as:

$$E_T[\rho(\mathbf{r})] = T[\rho] + \frac{1}{2}\int\int \frac{2\rho(\mathbf{r})\rho(\mathbf{r}')}{|\mathbf{r}-\mathbf{r}'|}\mathbf{dr}\mathbf{dr}' + E_{xc}[\rho] + \int V(\mathbf{r})\rho(\mathbf{r})\mathbf{dr} + E_{c-c} \quad (3.1)$$

where $T[\rho]$ represents the kinetic energy of a system of non-interacting electrons of density ρ, the second term the electronic Hartree energy, the third term the exchange correlation energy, the fourth term the electron-core interaction energy (V(r) is the external potential, in this case the potential due to the cores), and the last term represents the core-core interaction.

Within the LDA, the exchange-correlation functional is expressed as:

$$E_{xc}[\rho(\mathbf{r})] = \int \epsilon_{xc}(\rho(\mathbf{r}))\mathbf{dr}, \quad (3.2)$$

where $\epsilon_{xc}(\rho(\mathbf{r}))$ is the exchange-correlation energy per electron of an uniform electron gas of density $\rho(\mathbf{r})$. $\epsilon_{xc}(\rho(\mathbf{r}))$ is not known exactly for an arbitrary charge density, but approximations such as Hedin-Lundqvist local exchange-correlation potential [114], the Wigner interpolation formula [116], and analytical fit to Ceperley-Alder's Monte Carlo results [117] are often used. We use in this thesis the Hedin-Lundqvist form for the exchange-correlation functional in the calculation of alloys, and Wigner form for surfaces.

The variational principle, which is demonstrated in the second statement of the Hohenberg-Kohn theorem [102], together with the local density approximation results

in the following set of equations (in atomic units):

$$[-\nabla^2 + V_{eff}]\psi(\mathbf{r}) = \epsilon_i \psi(\mathbf{r}), \tag{3.3}$$

$$\rho(\mathbf{r}) = \sum_{i=1}^{N} n_i |\psi(\mathbf{r})|^2, \tag{3.4}$$

where n_i is the occupation number of state i and N is the total number of electrons in the system.

The effective potential, V_{eff}, is given by:

$$\begin{aligned} V_{eff}[\rho(\mathbf{r})] &= V_c(\mathbf{r}) + V_H(\mathbf{r}) + V_{xc}(\mathbf{r}) \\ &= V_c(\mathbf{r}) + \int \frac{2\rho(\mathbf{r}')}{|\mathbf{r} - \mathbf{r}'|} d\mathbf{r}' + \frac{\delta(E_{xc}[\rho(\mathbf{r})])}{\delta\rho(\mathbf{r})} \end{aligned} \tag{3.5}$$

These equations are to be solved self-consistent for the charge density $\rho(\mathbf{r})$, which in turn will determine the ground state properties of the system under consideration.

Up to this point, the density functional (DF) formalism together with the local density approximation (LDA) basically reduces a many body problem to solving a set of one-particle Schrödinger-like equations.

Momentum-space Formalism for the Total Energy of Solids

A momentum-space formalism for calculating the total energy of solids designed particularly for application with the self-consistent pseudopotential method was first derived by Ihm, Zunger, and Cohen [81]. Assuming non-overlapping ion cores, Equation (3.1) can be written in atomic units as:

$$\begin{aligned} E_T = \sum_i n_i < \psi_i | -\nabla^2 | \psi_i > + \frac{1}{2} \int\int \frac{2\rho(\mathbf{r})\rho(\mathbf{r}')}{|\mathbf{r} - \mathbf{r}'|} d\mathbf{r} d\mathbf{r}' \\ + \int \epsilon_{xc}(\rho(\mathbf{r})) d\mathbf{r} + \sum_{\mathbf{R},\tau} [\int \rho(\mathbf{r}) V_{ps}^L(\mathbf{r} - \mathbf{R} - \tau) d\mathbf{r} \end{aligned} \tag{3.6}$$

$$+\sum_{i,l} n_i < \psi_i | V_{ps,l}^{NL}(\mathbf{r}-\mathbf{R}-\tau)\hat{P}_l|\psi_i >]$$

$$+\frac{1}{2}\sum_{\mathbf{R},\mathbf{R}',\tau,\tau'}{}' \frac{2Z_V^2}{|\mathbf{R}+\tau-\mathbf{R}'-\tau|}$$

where the prime in the summation means the $|\mathbf{R}+\tau-\mathbf{R}'-\tau'|=0$ term is excluded; $\mathbf{R}$ denotes the lattice vector; τ denotes the basis vector; Z_V is the effective ionic charge; and V_{ps}^L is the local part of the pseudopotential that acts equally on all the angular momentum components of the wave-function. The non-local part defined as:

$$V_{ps,l}^{NL}(\mathbf{r}) = V_{ps,l}(\mathbf{r}) - V_{ps}^L(\mathbf{r}), \tag{3.7}$$

where $V_{ps,l}$ and $\hat{P}_l$ are the core pseudopotential and the projection operator for angular momentum l, respectively.

Thus, the long range part (singular part) of the pseudopotential has been isolated into the local part, making $V_{ps,l}^{NL}$ short range.

To simplify equation (3.6), we multiply on the left of equation (3.3) by $\psi_i^*(\mathbf{r})$, integrate over $\mathbf{r}$ and sum over i, and substitute it into equation (3.1). The total energy per primitive cell becomes in reciprocal space:

$$E_T = 2\sum_{n\mathbf{k}}^{(occ.)} w_{\mathbf{k}}\epsilon_{n\mathbf{k}} - \Omega_{cell}[\frac{1}{2}\sum_{\mathbf{G}}\frac{8\pi|\rho(\mathbf{G})|^2}{|\mathbf{G}|^2} \tag{3.8}$$

$$+\sum_{\mathbf{G}}\rho(\mathbf{G})(\varepsilon_{xc}(\mathbf{G})-v_{xc}(\mathbf{G}))] + \frac{1}{2}\sum_{\mathbf{R},\tau,\tau'}{}' \frac{2Z_V^2}{|\mathbf{R}+\tau-\tau'|}$$

The first term is the sum of the occupied band energies, $w_{\mathbf{k}}$ is the weight of each sampled k-point, and n is the band index, Ω_{cell} is the volume of the primitive cell, and $\mathbf{G}$ denotes the reciprocal lattice vector.

In practice, some mathematical manipulations are necessary to calculate E_T from equation (3.8) because $V_{Coul}(0)$, $V_{ps}(0)$ and $\frac{1}{2}\sum_{\mathbf{R},\tau,\tau'}\frac{2Z_V^2}{|\mathbf{R}+\tau-\tau'|}$ are individually divergent quantities. First we solve the band-structure eigenvalue problem, with $V_{Coul}(0)$ and $V_{ps}(0)$ set equal to zero. This corresponds to a constant shift of the potential. To compensate for the arbitrary shift we add $(\alpha_1 Z + \gamma_{Ewald})$ to the total Energy. γ_{Ewald} is the Coulomb interaction energy of the positive ion cores together with the neutralizing homogeneous background, and can be evaluated using the Ewald method [118]. α_1 is give by

$$\alpha_1 = \frac{N_a}{\Omega_{at}}\int(V_{ps}^L(\mathbf{r}) + \frac{2Z_V}{r})\mathbf{dr}, \tag{3.9}$$

where N_a is the number of atoms per primitive cell and Ω_{at} is the atomic volume.

The final expression for the total energy per unit cell is:

$$E_T = 2\sum_{n\mathbf{k}}^{(occ.)} w_{\mathbf{k}}\epsilon_{n\mathbf{k}} - \Omega_{cell}[\frac{1}{2}\sum_{|\mathbf{G}|\neq 0}\frac{8\pi|\rho(\mathbf{G})|^2}{|\mathbf{G}|^2} \tag{3.10}$$
$$+\sum_{\mathbf{G}}\rho(\mathbf{G})(\varepsilon_{xc}(\mathbf{G}) - v_{xc}(\mathbf{G}))] + (\alpha_1 Z + \gamma_{Ewald})$$

Equation (3.10) is rewritten to facilitate the self-consistent calculations as follows:

$$E_T = \sum_{n\mathbf{k}} f_{n\mathbf{k}}\epsilon_{n\mathbf{k}} - \Omega_{cell}\sum_{\mathbf{G}}\rho(\mathbf{G})V_{sc}^{in}(\mathbf{G}) + \Omega_{cell}\frac{1}{2}\sum_{|\mathbf{G}|\neq 0}\frac{8\pi|\rho(\mathbf{G})|^2}{|\mathbf{G}|^2} \tag{3.11}$$
$$+\Omega_{cell}\sum_{\mathbf{G}}\rho(\mathbf{G})\varepsilon_{xc}(\mathbf{G}) + (\alpha_1 Z + \gamma_{Ewald}),$$

where $f_{n\mathbf{k}}$ in the first term is the weight of each state, and V_{sc}^{in} in the second term is the reciprocal space component of the input screening potential for the self-consistent band calculation given by

$$V_{sc}^{in}(\mathbf{G}) = \frac{8\pi\rho(\mathbf{G})}{|\mathbf{G}|^2} + v_{xc}(\mathbf{G}) \tag{3.12}$$

Mixed-basis Approach to the Electronic Structure

In most band-theoretical methods, the electronic wave-function is expanded in a set of basis functions and the solutions to the Schrödinger equation are obtained by variational procedures. It is important to choose a small, yet physically complete, set of functions. For the systems we are dealing with, the localized character of the d electrons makes the expansion for the wave-functions in plane waves uneconomical. In order to treat a system such as this, with atomic-like character as well as extended plane-wave-like character, an energy-independent basis set containing both plane waves and Bloch sums of localized orbitals are used to represent the electronic wave-functions [119].

$$\psi_{n\mathbf{k}}(\mathbf{r}) = \frac{1}{\sqrt{\Omega}} \sum_{\mathbf{G}} \alpha_n(\mathbf{k}+\mathbf{G}) e^{i(\mathbf{k}+\mathbf{G})\cdot\mathbf{r}} + \sum_{jm} \beta_{jm}(n,\mathbf{k}) \phi_{jm}(\mathbf{k},\mathbf{r}), \tag{3.13}$$

with

$$\phi_{jm}(\mathbf{k},\mathbf{r}) = \frac{1}{\sqrt{N}} \sum_{\mathbf{R}} e^{i\mathbf{k}\cdot(\mathbf{R}+\tau_j)} f_{jm}(\mathbf{r}-\mathbf{R}-\tau_j) \tag{3.14}$$

In these equations, Ω is the crystal volume, N is the number of atoms, and m is the label for the orbital on the j^{th} atom. In many cases, we use for $f_{jm}(\mathbf{r})$ Gaussian local orbitals of the form:

$$f_m(\mathbf{r}) = N' r^2 e^{-\lambda r^2} Y_{2m}(\hat{r}), \tag{3.15}$$

to represent the localized part of the d electronic wavefunction, where N is the normalization constant, and λ is the Gaussian exponent.

In the cases of silver and gold, due to the fact that the 4d and 5d states are very localized, we have used for the local orbitals a numerical basis of the form:

$$f'(r) = Bf(r)[1 - exp[-\alpha(r_c - r)^2]], r \leq r_c \tag{3.16}$$

$$= \quad 0, r > r_c$$

where $f(r)$ is a radial function closely related to the radial distribution of the atomic d wave function, B is a normalization constant, and α is determined variationally [120, 121].

This mixed-basis leads to the following matrix eigenvalue problem:

$$(H - ES)\Lambda = 0, \tag{3.17}$$

where H is the Hamiltonian matrix, S is the overlap matrix, and Λ is a column vector with elements λ_1,...,λ_n corresponding to the expansion coefficients α, β in equation (3.12)

When evaluating the matrix elements involving the local orbital, if we are using the Gaussian as local orbital we make use of the on-site approximation [119], but when using the numerical basis, the "on-site" approximation becomes exact if r_c is smaller than the nearest-neighbor distance.

The valence charge density is then calculated from:

$$\rho(\mathbf{r}) = 2\sum_{n\mathbf{k}} \theta(\varepsilon_f - \varepsilon_{n\mathbf{k}})|\psi_{n,\mathbf{k}}(\mathbf{r})|^2, \tag{3.18}$$

where $\theta(x)$ is the step function and ε_f is the Fermi energy and is determined from the number of electrons per primitive cell, z, by the equation:

$$z = 2\sum_{n\mathbf{k}} \theta(\varepsilon_f - \varepsilon_{n\mathbf{k}}) \tag{3.19}$$

In practice, the k summation is restricted to the irreducible part of the Brillouin zone determined by symmetry and only the part of the charge density invariant under all the space group operations is retained.

Dielectric Matrix Scheme for Fast Convergence

The one-electron wave-functions are obtained from the Schrödinger equation:

$$(-\nabla^2 + V)\psi_{n\mathbf{k}} = E_{n\mathbf{k}}\psi_{n\mathbf{k}}, \tag{3.20}$$

where the crystal potential V is constructed as the sum of three components V_{ion}, V_H, and V_{xc}. V_{ion} is the superposition of the potentials due to the bare ions on the various atomic sites, V_H is the Hartree potential, and V_{xc} is the local exchange-correlation potential. V_H, and V_{xc} are obtained from the electronic density ρ by the following equations:

$$\nabla^2 V_H = -4\pi e^2 \rho(\mathbf{r}), \tag{3.21}$$

$$V_{xc}(\mathbf{r}) = -\beta(3/\pi)^{1/3} e^2 \rho(\mathbf{r})^{1/3} \tag{3.22}$$

where β can be a constant or a function of $\rho(\mathbf{r})$ [114, 122]. We start with an initial guess V_{in} for $V_H + V_{xc}$, and find the solution of equation (3.20). With these wave-functions we can obtain the electron density using equation (3.18) that we write here again:

$$\rho(\mathbf{r}) = 2\sum_{n\mathbf{k}} f_{n\mathbf{k}} |\psi_{n,\mathbf{k}}(\mathbf{r})|^2, \tag{3.23}$$

where $f_{n\mathbf{k}}$ is the occupation factor and 2 is the spin factor. From this electron density, the Hartree screening potential and the exchange-correlation (Hedin-Lundqvist form [114]) potential of the electrons are calculated. With these two potentials, an output potential V_{out} is constructed. Self-consistency requires that this procedure

be repeated until V_{in} is equal to V_{out}. Usually this is achieved by putting in a new V_{in} constructed by mixing the old V_{in} and V_{out} as following:

$$V_{in}^{new}(\mathbf{G}) = cV_{in}^{old}(\mathbf{G}) + (1-c)V_{out}^{old}(\mathbf{G}) \tag{3.24}$$

where the mixing coefficient, c, is a function of $\mathbf{G}$ which corresponds to screening the charge density oscillation by a Fermi-Thomas type dielectric function. However, for surface calculations, with large unit cell, the low $\mathbf{G}$ components of the potential converge very slowly and, furthermore, the various Fourier components are found to be strongly coupled so that a simple mixing scheme like the one above is no longer adequate.

Ho *et al.* [104] devised a scheme that drastically reduces the number of iterations required to reach self-consistency in electronic-structure calculations. Suppose the input and output potentials for the nth iteration are V_{in} and V_{out} respectively. We want δV_{in} such that:

$$V_{in} + \delta V_{in} = V_{out} + \delta V_{out} \tag{3.25}$$

δV_{out} can be expressed in terms of δV_{in} using perturbation theory,

$$\delta\rho(\mathbf{G}) = \frac{1}{\Omega_c}\sum_{\mathbf{G}'}\chi(\mathbf{G},\mathbf{G}')\delta V_{in}(\mathbf{G}'), \tag{3.26}$$

where Ω_c is the cell volume, and the susceptibility χ is given by:

$$\chi(\mathbf{G},\mathbf{G}') = -2\sum_{n,n',\mathbf{k}}(f_{n,\mathbf{k}} - f_{n',\mathbf{k}'})\frac{<n\mathbf{k}|e^{-i\mathbf{G}\cdot\mathbf{r}}|n'\mathbf{k}><n'\mathbf{k}|e^{i\mathbf{G}'\cdot\mathbf{r}}|n\mathbf{k}>}{E_{n',\mathbf{k}} - E_{n,\mathbf{k}}} \tag{3.27}$$

We know that

$$\delta V_{out} = \delta V_H + \delta V_{xc} \tag{3.28}$$

where δV_H and δV_{xc} can be derived from equations (3.21) and (3.22). Using equations (3.24), (3.25) and (3.26) we obtain:

$$\sum_{\mathbf{G},\mathbf{G}'} \epsilon(\mathbf{G},\mathbf{G}')\delta V_{in}(\mathbf{G}') = V_{out}(\mathbf{G}) - V_{in}(\mathbf{G}), \tag{3.29}$$

$$\epsilon(\mathbf{G},\mathbf{G}') = \delta(\mathbf{G}-\mathbf{G}') - \frac{1}{\Omega}\sum_{\mathbf{G}''} v_{xc}(\mathbf{G}-\mathbf{G}'')\chi(\mathbf{G}'',\mathbf{G}') - \frac{8\pi}{G^2\Omega}\chi(\mathbf{G},\mathbf{G}') \tag{3.30}$$

where $v_{xc}(\mathbf{G})$ is the Fourier transform of the exchange correlation interaction $v_{xc}(\mathbf{r})$, which is the functional derivative of the exchange-correlation potential:

$$v_{xc} = \frac{\delta V_{xc}}{\delta \rho} \tag{3.31}$$

Thus, given V_{out}, and V_{in}, we can obtain δV_{in} by a matrix inversion.

Since only the low Fourier components are strongly coupled, it is only necessary to calculate $\epsilon(\mathbf{G},\mathbf{G}')$ for only few stars of reciprocal lattice vectors.

Hellmann-Feynman Forces

The use of the Hellmann-Feynman theorem helps us minimize the number of trial geometries needed to determine the equilibrium geometry, and allow us to relax all the layers simultaneously. It was first proved for the case of the all-electron problem [105], and then extended to the case of pseudopotential calculations [81]. We start with the expression for the total energy per primitive unit cell given in equation (3.11), and suppose that the position of one of the atoms in the unit cell is changed by a displacement $\delta\tau$. This change in the displacement causes a change in the total energy given by:

$$\delta E_T = \sum_{n\mathbf{k}} (f_{n\mathbf{k}} \delta\epsilon_{n\mathbf{k}} + \delta f_{n\mathbf{k}} \epsilon_{n\mathbf{k}}) - \Omega_{cell} [\sum_{\mathbf{G}} \rho(\mathbf{G}) \delta V_{sc}^{in}(\mathbf{G}) \tag{3.32}$$

$$+ \sum_{\mathbf{G}} \delta\rho(\mathbf{G}) (V_{sc}^{in}(\mathbf{G}) + \frac{8\pi|\rho(\mathbf{G})|^2}{|\mathbf{G}|^2} + v_{xc}(\mathbf{G}))] + \delta\gamma_{Ewald}.$$

because the self-consistency criteria guarantees that

$$V_{sc}^{in}(\mathbf{G}) = \frac{8\pi\rho(\mathbf{G})}{|\mathbf{G}|^2} + v_{xc}(\mathbf{G}) \tag{3.33}$$

the term involving $\delta\rho(\mathbf{G})$ drops out, and equation (3.28) becomes:

$$\delta E_T = \sum_{n\mathbf{k}} (f_{n\mathbf{k}} \delta\epsilon_{n\mathbf{k}} + \delta f_{n\mathbf{k}} \epsilon_{n\mathbf{k}}) - \Omega_{cell} \sum_{\mathbf{G}} \rho(\mathbf{G}) \delta V_{sc}^{in}(\mathbf{G}) + \delta\gamma_{Ewald}. \tag{3.34}$$

To evaluate the first term in equation (3.30) (the change in band energies) we use perturbation theory:

$$\begin{aligned} \sum_{n\mathbf{k}} f_{n\mathbf{k}} \delta\epsilon_{n\mathbf{k}} &= \sum_{n\mathbf{k}} (f_{n\mathbf{k}} < \psi_{n\mathbf{k}} | \delta V_{ion} + \delta V_{sc}^{in} | \psi_{n\mathbf{k}} > \\ &= \sum_{n\mathbf{k}} (f_{n\mathbf{k}} < \psi_{n\mathbf{k}} | \delta V_{ion} | \psi_{n\mathbf{k}} > + \Omega_{cell} \sum_{\mathbf{G}} \rho(\mathbf{G}) \delta V_{sc}^{in}(\mathbf{G}), \end{aligned} \tag{3.35}$$

where δV_{ion} is the change in the ionic potential:

$$V_{ion}(\mathbf{r}) = \sum_{\mathbf{R},\tau,\mathbf{l}} V_{ps,l}(\mathbf{r} - \mathbf{R} - \tau) \hat{P}_l. \tag{3.36}$$

Using equations (3.30) and (3.31) we can calculate the force on each atom. This force can be divided into two terms:

$$\mathbf{F} = \frac{-\delta E_T}{\delta\tau} = \mathbf{F}_{ion} + F_{el}, \tag{3.37}$$

where

$$\mathbf{F}_{ion} = -\frac{\delta\gamma_{Ewald}}{\delta\tau}, \tag{3.38}$$

$$F_{el} = -\sum_{n\mathbf{k}}(f_{n\mathbf{k}} < \psi_{n\mathbf{k}}|\frac{\delta V_{ion}}{\delta\tau}|\psi_{n\mathbf{k}} > + \frac{\delta f_{n\mathbf{k}}}{\delta\tau}\epsilon_{n\mathbf{k}}) \tag{3.39}$$

$\mathbf{F}_{ion}$ is the ionic restoring force, and $\mathbf{F}_{el}$ is the electronic force which is made up of contributions from all the occupied states.

Calculational Procedures

In this section, we describe the calculation procedures used in the self-consistent band calculations.

1. Choose the initial position of the atoms (most of the times we use the coordinates of the atoms at the ideal bulk positions for the initial positions).

2. Solve for the eigenvalues and the wavefunctions via equation (3.3) in the mixed basis approach. Our basis contains plane waves with energy $|\mathbf{k}+\mathbf{G}|^2$ up to certain E_{cut}, and a set of Gaussian or a numerical basis as local orbitals.

3. Determine the band occupancy for each sampled **k**-point in the irreducible Brillouin zone (IBZ), and calculate the Fermi Energy using equation (3.19).

4. The total pseudo valence charge density is calculated via equation (3.18). The charge density is expanded in reciprocal space with approximately 2300 plane waves for Au, and 8000 plane waves for Ag. From the charge density, the Hartree screening potential and the exchange-correlation energy (Wigner or Hedin-Lundqvist form) of the electrons is calculated.

5. At each iteration step n, a new input potential for the (n+1)th iteration is obtained using the dielectric matrix scheme.

6. The total ground state energy is calculated using equation (3.11).

   We repeat steps 2 through 6, until self-consistency is achieved ($V_{in} = V_{out}$). After that, forces on each atom are calculated using the Hellmann-Feynman theorem. The use of Hellmann-Feynman forces minimizes the number of trial geometries needed to determine the equilibrium geometry, especially because all the layers are relaxed simultaneously.

7. With the forces calculated before, the new positions of the atoms are predicted. Using the forces calculated from few first geometries, we deduce a force-constant matrix that couples the different layers, and guides us in choosing the new position of the atoms.

In Figure 3.1 a diagram of this self-consistency loop is shown.

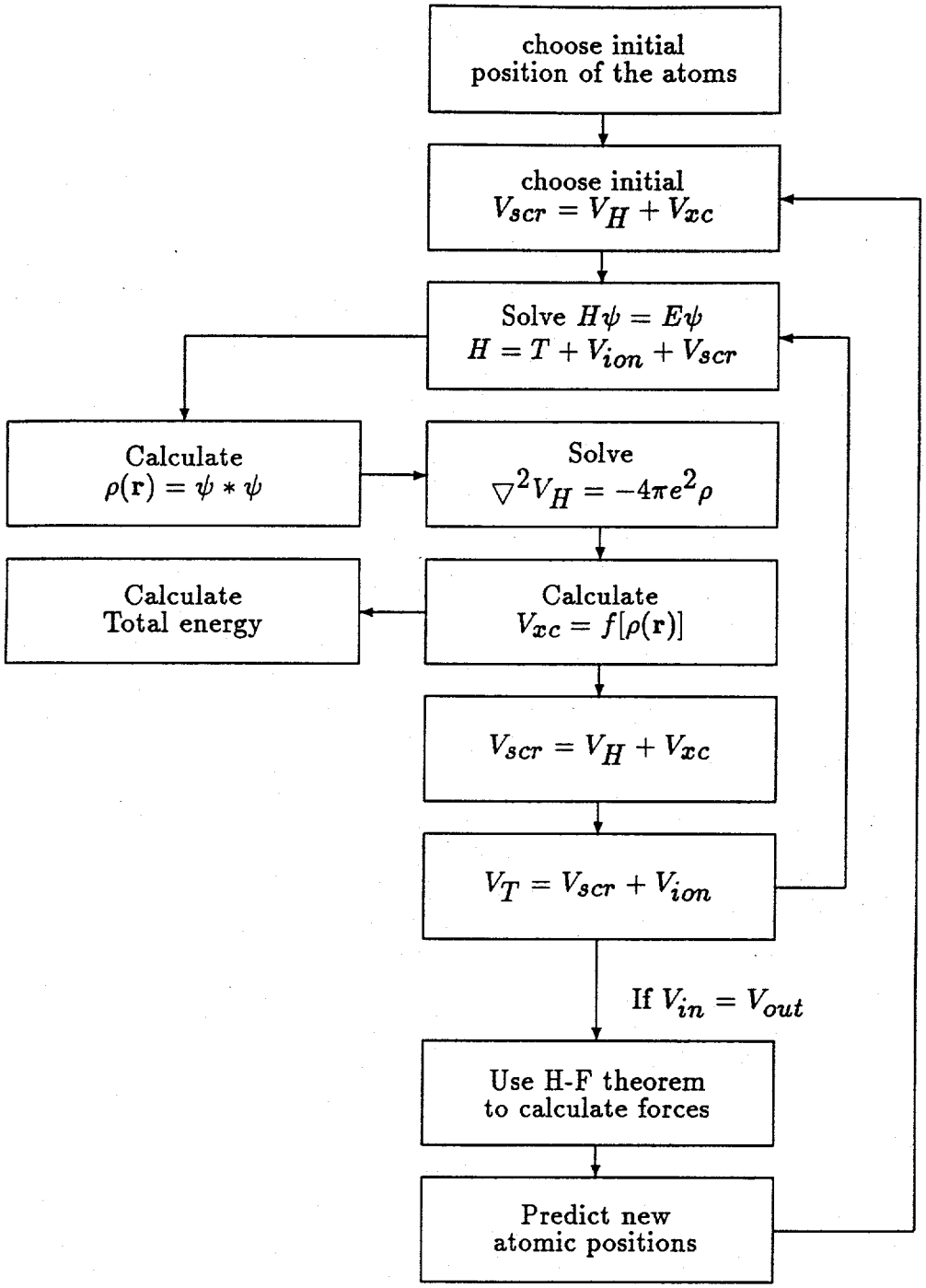

Figure 3.1: Schematic chart of the self-consistent procedure

CHAPTER 4. THE $(\sqrt{3} \times \sqrt{3})$ $R30^\circ$ Ag/Si(111) SURFACE

Introduction

As has been mentioned in Chapter 1, the atomic geometry of the $(\sqrt{3} \times \sqrt{3})$ structure observed during the adsorption of Ag on Si(111) is a problem that has baffled surface scientists for over a decade [1-44]. Many experimental techniques, which include low and medium energy ion-scattering and impact-collision ion scattering spectroscopy (ISS, MEIS, ICISS) [3-12], high-energy ion channeling [13], LEED [14-16], reflection high energy electron diffraction (RHEED) [17-19], X-ray diffraction and X-ray standing wave (XRD,XSW) [20-25], Auger electron spectroscopy (AES) [26-29], X-ray photoelectron diffraction (XPD) [30-33], photoemission [34-37], surface extended X-ray absorption fine-structure spectroscopy (SEXAFS) [38], scanning tunneling microscopy (STM) [39-42], and scanning and reflection electron microscopy (SEM, REM) [43, 44], together with some theoretical efforts [63-68], have been used to study the surface. However, the surface structure remains elusive. The main complexity of the problem comes from the large number of plausible and conflicting models that have been proposed for this surface, each model having support from some experiments.

Using first principles total energy calculations, we have examined the equilibrium geometries and electronic properties for many plausible models. We found a struc-

tural model [67] which not only has the lowest surface energy but can also explain most of the available experimental data on the system. In particular, we find that the honeycomb structure observed in STM images arises not from the top layer atomic positions but rather from the wavefunction behavior of empty surface electronic states above the Fermi level.

First-principles Calculations

We have used in our calculations non-local ionic pseudopotentials generated using the norm-conserving scheme of Hamann, Schlüter, and Chiang [112]. The total energies are calculated within the local-density-functional formalism [102] with the Wigner form [116] of the local exchange-correlation energy. The wave-functions are expanded by means of an efficient mixed-basis set [119] consisting of plane waves with energy $(\mathbf{k}+\mathbf{G})^2$ up to 10.5 Ry plus a set of localized functions centered at the atomic sites to describe the d orbitals. For Ag, due to the fact that the 4d are tightly bound states, we use for the local orbitals numerical functions which are more flexible and hence can better represent the local orbitals. The shape of the local orbitals, described by equation (3.16), is determined variationally [120, 121]. The optimized values for α and r_C are 0.70 and 2.70 a.u., respectively. The pseudo-potential mixed-basis method has been used in previous investigations of the structural properties of bulk Si and Ag and of the reconstruction of the Ag(110) surface with excellent results [100, 120]. The theoretical results of bulk properties obtained by this method are compared with the experimental results in Table 4.1.

A slab of Si(111) layers is used to describe the Si(111) surface. Ag atoms are added to the slab surfaces. Periodicity along the direction perpendicular to the sur-

Table 4.1: Comparison of the theoretical bulk properties of Si and Ag with experimental results.

Si	Theory	Experiment [134]
Lattice Constant (Å)	5.45	5.43
Bulk Modulus (Mbar)	0.92	0.99
Cohesive Energy (eV)	4.81	4.63

Ag	Theory	Experiment [134]
Lattice Constant (Å)	4.11	4.09
Bulk Modulus (Mbar)	1.04	1.00
Cohesive Energy (eV)	3.00	2.95

face is absent. As usual in surface calculations, an artificial periodicity along this direction must be retained so that we can use the well-established tools of the pseudopotential theory to obtain the electronic structure of our system. This artificial periodicity is achieved by utilizing the "supercell" technique [83]. The "supercell" used in our calculation has 6 layers of Si beneath the Ag layer, plus a vacuum region above the Ag layer. The length of the whole cell in the $< 111 >$ direction is equivalent to the thickness of 12 Si(111) layers. The thickness of the vacuum and the substrate layers has been tested to be large enough so that the influence of the mutual interaction between slabs are small for the quantities we are interested. The effect of vacuum thickness on the total energy result is less than 1.5 mRy per atom (equivalent to 0.02 eV/atom). Its effect on surface energy which we will use to compare different structural models will be even smaller, and it will not affect the accuracy of the comparison.

If the Ag layer is in an embedded geometry, there are additional Si atoms above the Ag layer, which results in 8 Si layers in the the supercell. We have repeated the calculation for some models with different number of layers in the Si slab. By comparing the results of the same model calculated with 6-layer and 8-layer Si slabs (both fully relaxed), the error in surface energy due to finite slab thickness is estimated to be about 7 mRy per surface atom (equivalent to 0.1 eV/surface-atom or 0.1 J/m^2), which will not affect the accuracy of the surface energy comparison between different structural models.

In the calculation of electronic charge density during the iteration to self-consistency, we use an even-spaced sampling grid of 7 k-points in the irreducible wedge of the 2-D surface Brillouin zone (SBZ) (Figure 4.1). In order to check if this many k-points

are enough for an accurate energy result, we have repeated the calculation for some models with 15 k-points in the SBZ. The total energy difference is less than 2 mRy (0.03 eV) per atom, which is small. Forces on the atoms are calculated for each model and the atoms are fully relaxed (laterally and vertically) to their zero-force equilibrium positions within the symmetry constraints imposed by the model. In some cases, multiple starting configurations are tested to minimize the possibility of landing on local rather than global minimum.

Structural Models

The two basic quantities of the $\sqrt{3}$-Ag surface, the Ag coverage and the positions of Ag atomic layer relative to the Si top layer, have been at the center of the controversy from experiments. There is no consensus from experimentalists whether the Ag coverage is 1 monolayer (ML for short; 1 ML coverage is one adatom for each surface Si atom) or $\frac{2}{3}$ ML and whether the Ag atoms form the topmost layer or are embedded under a Si layer. Such uncertainties have given rise to numerous structural models. Even the same type of experimental techniques, such as STM [39, 40] and X-ray diffraction [20-24] studies, respectively, can yield different structural models, depending on how the results are interpreted.

The experimental models for $\sqrt{3}$-Ag can be divided into four groups by the different coverages and positions proposed for the Ag atoms: (i) $\frac{2}{3}$ ML Ag coverage models with a top Ag layer arranged in a honeycomb-like structure, which includes the simple honeycomb (HC) model [4, 40], and various "missing top layer" (MTL) models [19, 32, 36]; (ii) $\frac{2}{3}$ ML of Ag atoms forming a honeycomb embedded (EHC) in the first double layer of Si [3, 15, 38]. (iii) 1 ML Ag coverage models, with Ag

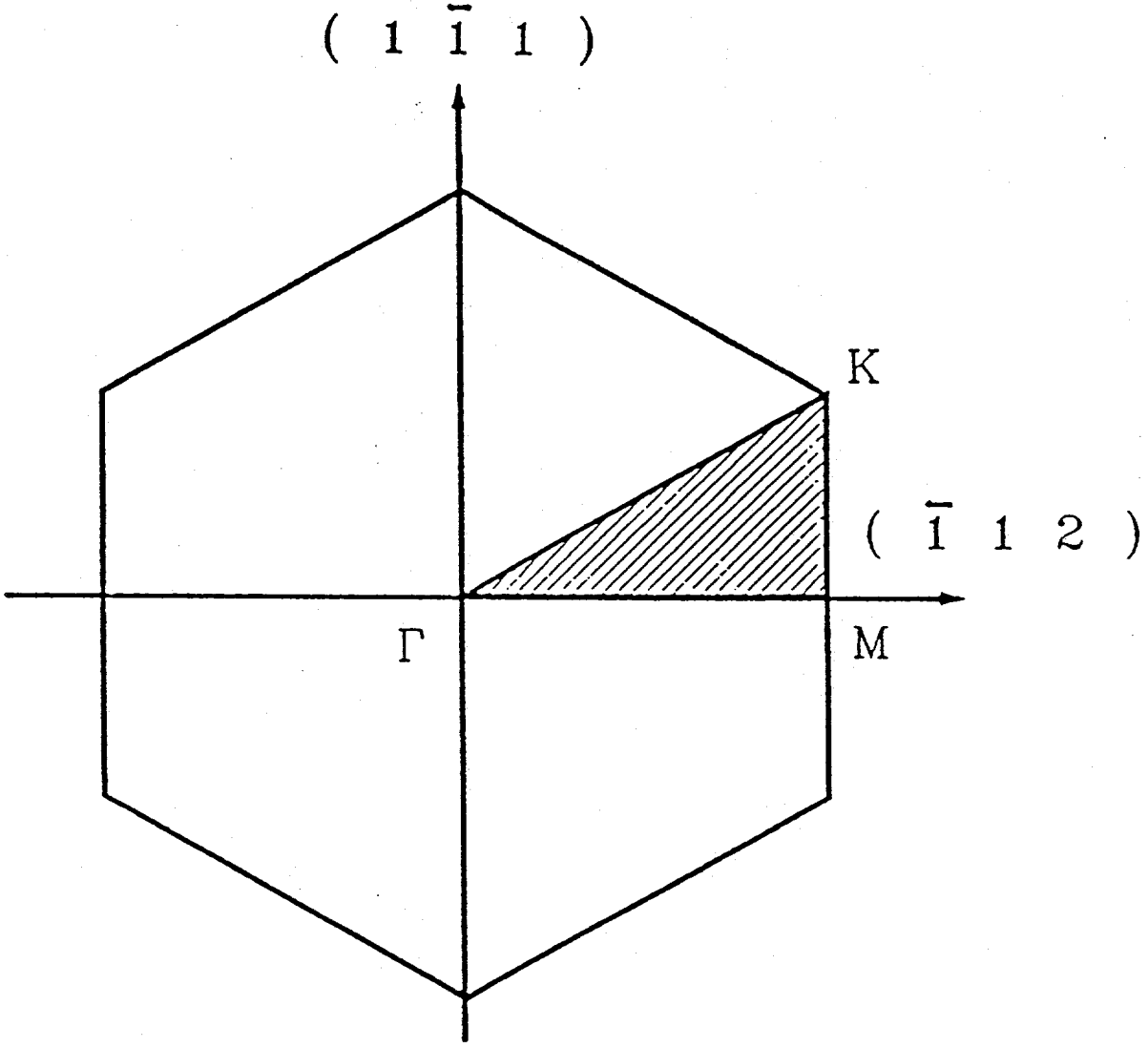

Figure 4.1: The 2-D Brillouin zone of Si(111) Surface. The irreducible parts of the Brillouin zone are shaded.

atoms embedded under a top honeycomb layer of Si (with $\frac{1}{3}$ vacancies), including the embedded trimer (ET) model [39], the substitutional trimer (ST) model [5], silver honeycomb-chained-trimer (SHCT) models of Vlieg et al. (Vlieg-II,III) [23], and silicon adatom-vacancy (SAV) model [7]; (iv) 1 ML of Ag atoms forming a top layer above all the Si atoms, with atop Ag trimers (AT) [14] or a honeycomb-chained-trimer (HCT) arrangement of the Ag layer [19-23].

In this study, we have examined many feasible models, including three of the four groups of the experimental models. For many of the models, different Ag registries are considered to locate the one with the lowest energy. The coverage and the position of the Ag layer of these models and their variations are listed in Table 4.2. To help visualize these models, we have plotted the ideally truncated Si(111) surface in Figure 4.2, both top view and side view, followed by Figure 4.3, in which all the structural models that we have investigated in this study for the $\sqrt{3}$-Ag surface are schematically shown. It should be noted that these are the initial non-reconstructed positions of the atoms. After they are fully relaxed, both the vertical and lateral positions will be changed, sometimes dramatically.

Since there are two possible coverages and hence different stoichiometries, the quantity that governs the relative stability of different models is, as we have mentioned previously, the surface energy per $(\sqrt{3} \times \sqrt{3})$ unit cell of the composite Ag/Si system. We define it to be

$$E_s = \frac{1}{2}(E_{tot} - N_{Ag}E_{Ag} - N_{Si}E_{Si}), \tag{4.1}$$

where E_{tot} is the total energy of the slab, N_{Ag} and N_{Si} are the number of Ag and Si atoms in the slab respectively, and E_{Ag} and E_{Si} are the total energy per atom of bulk Ag and Si. The factor half is because there are two surfaces in a slab. This

Table 4.2: Lists of structural models and their surface energies. The coverage is in the unit of ML, and the surface energy in the unit of J/m^2. (1 J/m^2 = 2.4 eV per $\sqrt{3} \times \sqrt{3}$ surface unit cell.)

Models	Ag coverage	Ag position	Surface Energy
HC	2/3	on top	1.394
MTL I	2/3	on top	1.439
MTL II	2/3	on top	1.510
ET-1	1	embedded	1.830
ET-2	1	embedded	2.670
ST-1	1	embedded	2.231
ST-2 (Vlieg II)	1	embedded	2.291
SHCT (Vlieg III)	1	embedded	3.308
HCT-1a	1	on top	0.879
HCT-1a$'$	1	on top	0.831
HCT-1a$''$	1	on top	0.689
HCT-1b	1	on top	0.857
HCT-1c	1	on top	0.824
HCT-2a	1	on top	1.620
HCT-2b	1	on top	1.426
HCT-2c	1	on top	1.317
CHCT	1	on top	1.290

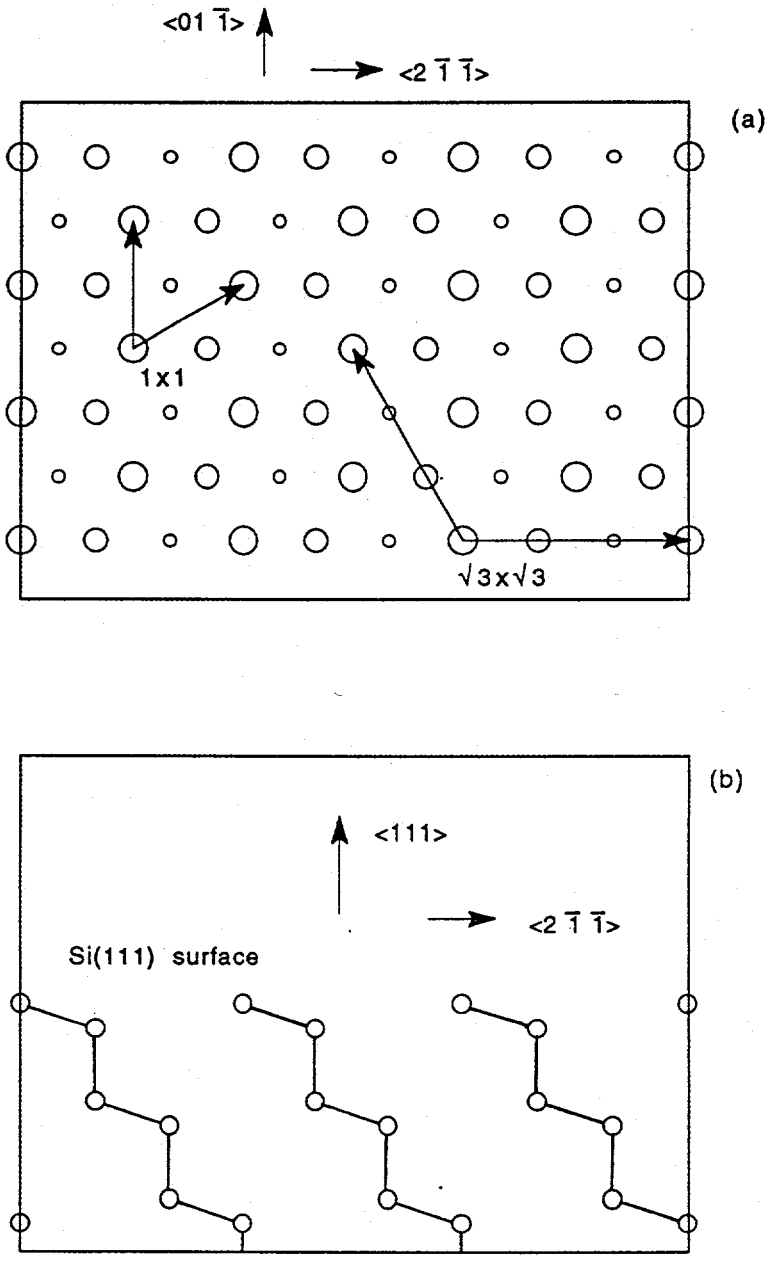

Figure 4.2: Top (a) and side (b) view of the ideally truncated Si(111) surface. The circles represent the Si atoms. In (a), the sizes of the circle decrease for lower layers. The (1×1) and the $\sqrt{3}$ unit cells are also drawn.

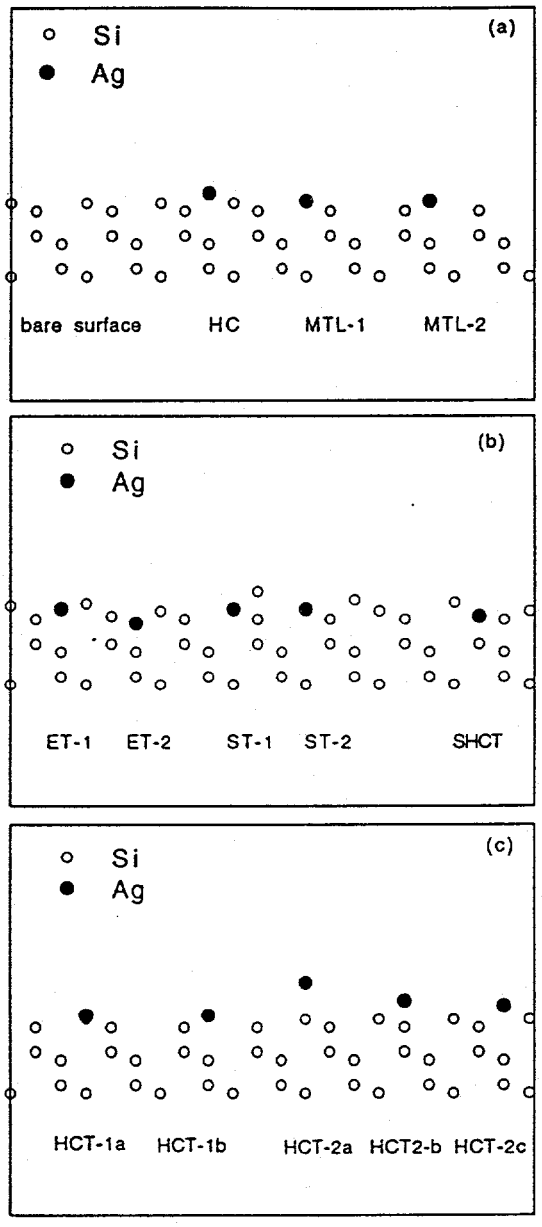

Figure 4.3: Side view of all the structural models considered for $\sqrt{3}$-Ag surface in our calculation.

definition is illustrated by Figure 4.4. In case (a) is a Si(111) surface wetted by a layer of metal atoms, while in case (b) the metal atoms forms 3D islands (and are assumed to be in a bulk crystalline environment) above the Si surface. The energy for (a) is the total energy of the slab: $E_a = E_{tot}$. The energy for (b) is the bulk energy of the metal, say Ag in our case, and the substrate Si, plus the surface energy of Si(111), assuming that the number of atoms on the surface is small compared with that in the bulk: $E_b = N_{Ag}E_{Ag} + N_{Si}E_{Si} + \gamma_{Si}$. The difference between these two

$$E_a - E_b = E_{tot} - N_{Ag}E_{Ag} - N_{Si}E_{Si} - \gamma_{Si} = E_s - \gamma_{Si} \tag{4.2}$$

measures the stability of surface (a) relative to (b), where γ_{Si} represents the surface energy of clean Si(111) surface. The relative stability among different models of different stoichiometries can be compared by considering the quantity E_s, if we assume that the $\sqrt{3}$ system is in equilibrium with bulk Ag (i.e. any excess Ag will form 3D islands, which is observed experimentally). In general, E_{Ag} in Equation (4.2) should be replaced by the chemical potential of Ag. The smaller its E_s is, the more energetically favorable the model should be. For Those models that have their E_s lower than γ_{Si}, i.e. $E_a < E_b$, the Ag atoms will wet the Si surface. The calculated surface energies of the three groups of structural models for the $\sqrt{3}$-Ag surface are listed in Table 4.2.

The first group of models that we have considered is the $\frac{2}{3}$ ML atop Ag models including HC and MTL models (Figure 4.3 (a)). For the MTL model, two different registries of the Ag atoms have been studied. One has the Ag atoms above the 5th layer of Si (MTL-1), and the other above the 3rd layer of Si (MTL-2). The first one has a lower surface energy by 0.07 J/m^2. In this group, the HC model has the lowest surface energy, which is 0.05 J/m^2 lower than MTL-1.

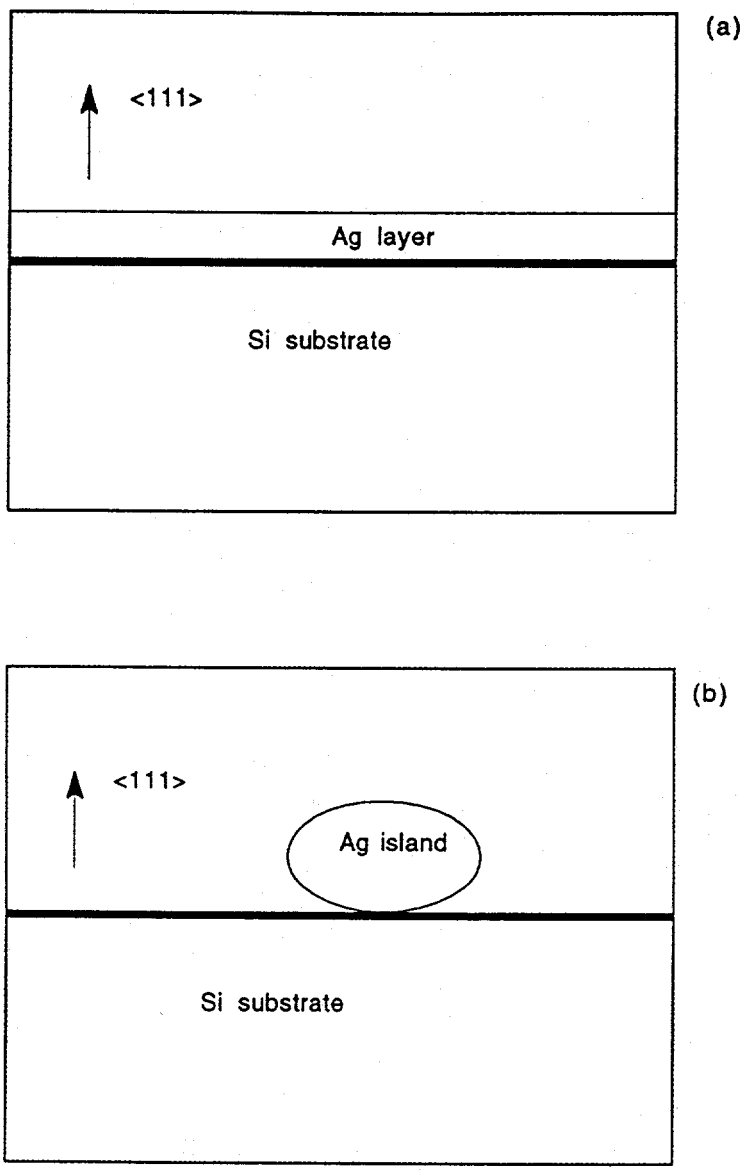

Figure 4.4: Illustration of surface energy definition for $\sqrt{3}$-Ag surface in our calculation.

The second group is the 1 ML embedded Ag models which includes the ET model, ST model, and two of Vlieg's models (see Figure 4.3 (b)). For this group, the topmost layer consists of $\frac{2}{3}$ ML Si atoms. In the ET model, the Ag atoms are positioned above the Si atoms of the 4th layer. In the ST models, the Ag atoms substitute the top layer of the intact double layers, while additional $\frac{2}{3}$ ML of Si adatoms are situated either above the second (ST-1) or above fourth (ST-2) Si layers. The second ST configuration is the same as the model II proposed by Vlieg, et al. Their model III (SHCT) has also been considered. The initial configuration of this model is shown in Figure 4.3 (b). The ET model has the lowest energy in this group, while the two ST models have approximately the same energy.

In both of the above groups, the top layer has a vacancy to account for the honeycomb STM images observed in experiments [39, 40]. For quite a long time, the bright spots in such honeycomb shaped images have been considered to indicate the positions of atoms in the topmost layer. The third group of structural models we have studied is the 1 ML atop Ag models in which there is no vacancy in the top layer, hence no honeycomb from the atomic positions. This group includes the various configurations of the HCT model with different Ag registries or different Si substrate structures (Figure 4.3 (c)). We also investigated the CHCT model, which we have found is the best for Au/Si(111) surface (see Chapter 5).

The surface energy results for a number of models at their respective lowest energy configurations are compared in Figure 4.5. Experimental surface energy for (2×1)Si(111) is quoted from ref. [123]. Since there is no experimental data available for the surface energy of (7×7)Si(111), the result we use here is derived from (2×1)Si(111). Theoretical calculation has estimated that the surface energy of

(7×7)Si(111) surface is about 0.05 J/m^2 lower than that of the (2×1) surface [124]. The (1×1) Ag/Si(111) marked with (MTL) has a "missing-top-layer" Si substrate while the (1×1) Ag/Si(111) (unmarked) has an intact double-layer Si substrate. We found that all the models in the second group (1ML embedded Ag) tend to have much higher energies than models in the other groups due to the large number of Si bonds broken to make the top Si honeycomb layer. Some of the models (e.g. model III in Ref. [23]) have energies so high that they are not shown in Figure 4.5. We note that the HCT-1 model (it really means the lowest energy configuration of the HCT-1 models, see the next section) not only has a lower surface energy than all other competing models, but it is also the only class of model tested that has a surface energy lower than the reconstructed clean Si(111) surfaces. This indicates that the Ag atoms should wet the Si surface for at least one layer, before having 3D island growth on the surface, which is consistent with the observed Stranski-Krastanov growth mode of Ag layers on this surface.

HCT-1 Model

The lowest energy structure of the HCT-1 model is shown schematically in Figure 4.6 (a) (top view) and Figure 4.6 (b) (side view). The HCT-1 model is named after the HCT arrangement proposed for the Ag atoms by Takahashi, et al. from their X-ray diffraction experiment [20]. The special features of our theoretical model HCT-1 include, besides the HCT arrangement for Ag atoms, that the Si slab has an MTL structure and the first layer Si atoms form trimers beneath the top Ag layer, that the Ag atoms are above the 5th Si layer, and that the Ag trimers are centered above the third Si layer.

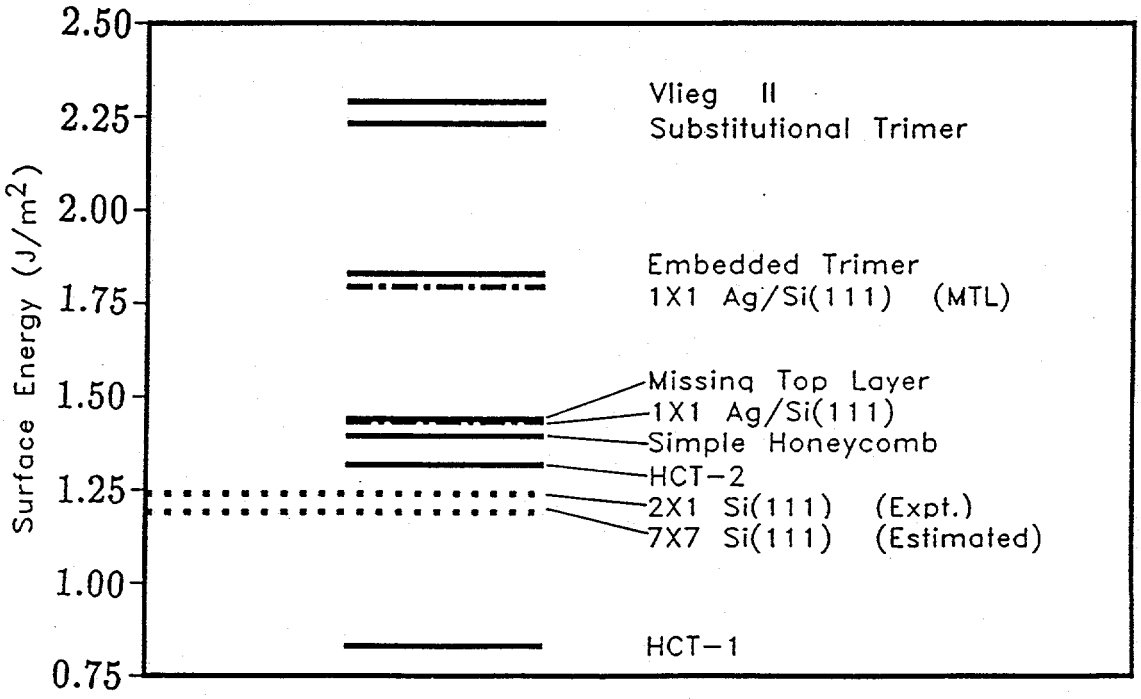

Figure 4.5: Comparison of the surface energies for various models.

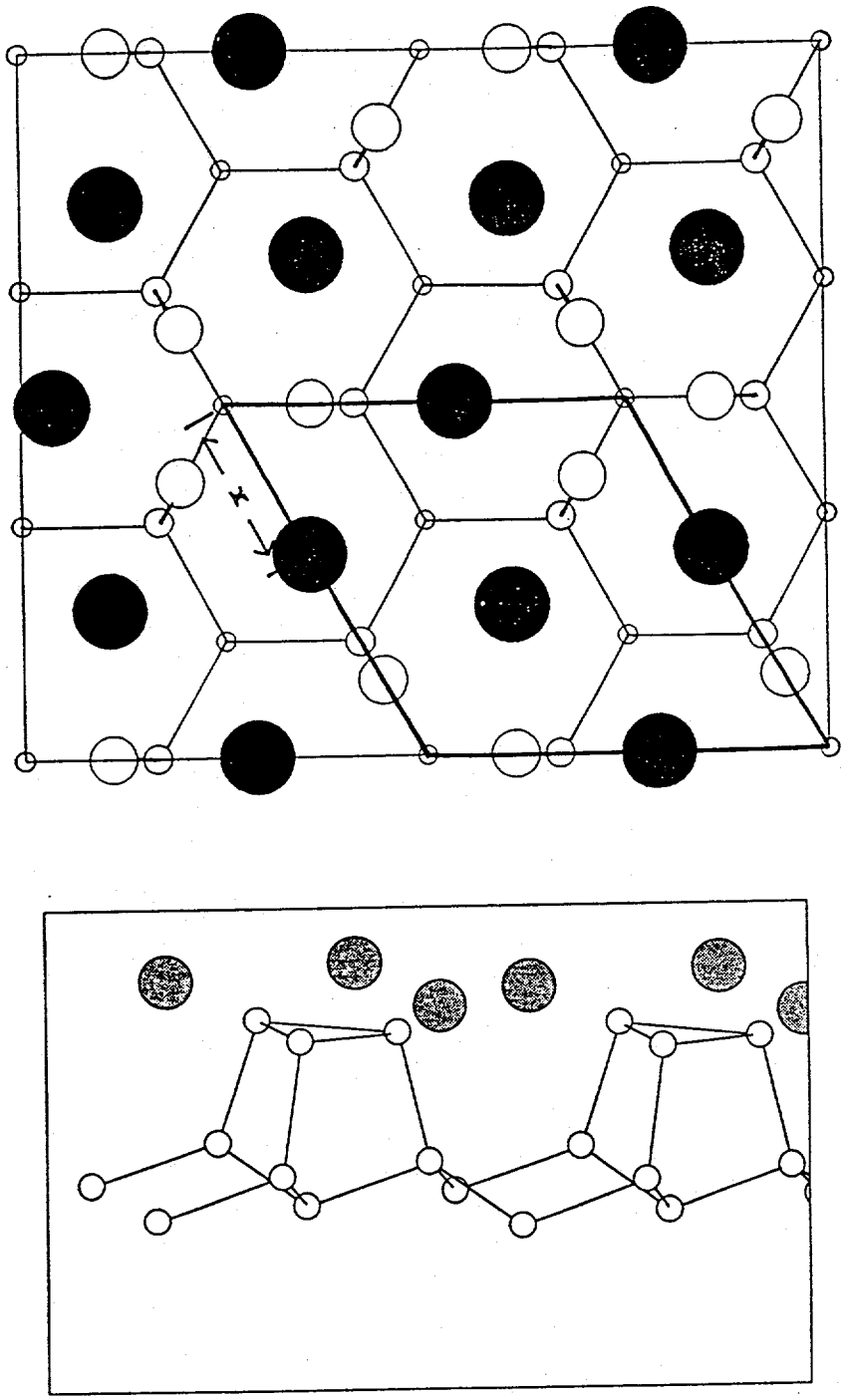

Figure 4.6: Geometrical structure of the HCT-1 model: (a) top view; (b) side view. Shaded and empty circles are Ag and Si atoms, respectively.

To insure that we have obtained the right configuration that has the lowest surface energy, we have done various tests to the HCT models. List in Table 4.2 are eight variations of HCT that we have studied. HCT-1a is the first one we considered, in which we have 6 layers of Si in the slab, plus 1 ML of Ag on top. Atoms in the same layers are put in the same vertical level along $< 111 >$ direction. However, all the Si atoms in the 3rd layer are not equivalent to each other in terms of symmetry. They do not have to be restricted in the same level during the relaxation. We take this into account in model HCT-1a$'$ by allowing the third layer Si atoms to buckle, and that lowers the surface energy by 0.05 J/m^2, which means the structure is more favorable. To further test the effect of slab thickness, we increase the slab from 6 layers to 8 layers, in model HCT-1a$''$. The deep layers are still allowed to buckle. The surface energy difference is found to be 0.14 J/m^2 between the 6-layer and 8-layer models (see Table 4.2). That is small compared with the energy difference between the HCT models and other models.

We have also investigated different registries of Ag atoms in the HCT models. In model HCT-1b, we take the same HCT arrangement for Ag atoms and the same MTL structure of the Si slab as in HCT-1a, but change the positions of Ag with respect to Si. The Ag atoms are now positioned above the third layer instead of the 5th layer of Si, and the Si atoms form trimers above the 5th layer. See Figure 4.7 (a) for a schematic picture of this model. As seen in Table 4.2, HCT-1b has a slightly higher surface energy than HCT-1a. The difference is small, therefore it may be possible that the two different registries co-exist, as observed in STM experiment [41].

Besides the HCT model proposed by Takahashi, et al., model II of Vlieg et al.

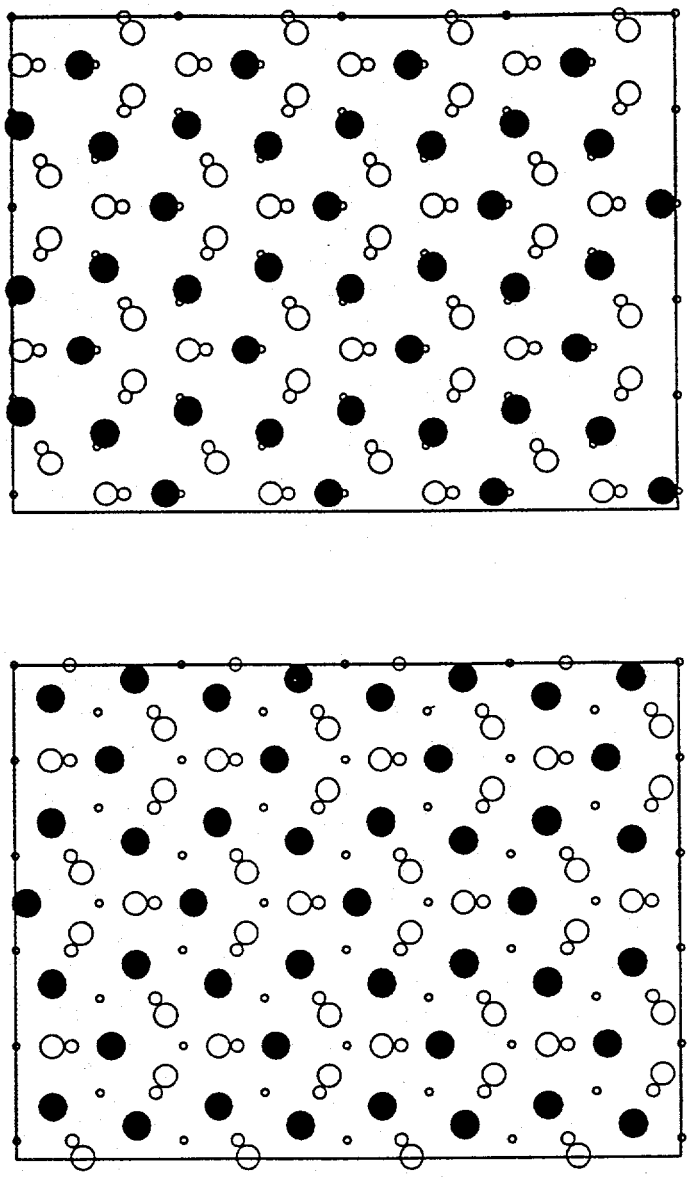

Figure 4.7: Variations of HCT-1 type models (top view). (a) HCT-1b; (b) HCT-1c.

[23] is equivalent to HCT-1a if the top Si honeycomb layer is discarded (see Figure 4.3). That extra layer of Si atoms makes the model less favorable energetically. Ichimiya's model [19] is also similar to HCT-1a except for an extra twisting of the Si trimers. In fact, we have tested Ichimiya's model by giving an initial rotation to the Si trimers and letting the system relax to a local minimum. That is HCT-1c as shown in Figure 4.7 (b). We see from Table 4.2 that the surface energy of HCT-1c is close to the model without rotation, but higher.

While experimental works and our theoretical calculation about the structure of the Ag atoms seem to be converging into the HCT arrangement, experimental data do not provide a conclusive structure for the underlying Si substrate. We have substituted the MTL structured Si substrate by an intact double layer Si substrate, and that give us models HCT-2. The first Si layer still form trimers. The HCT array of Ag atoms are positioned at three different positions as shown in Figure 4.3 (c). The top view of the resulted structures are indicated in Figure 4.8 (a-c). All the three configurations have a much higher energy than the HCT-1 group.

We have also considered more variations of the Si substrate structures and they all give higher energy. The CHCT model, which is borrowed from the $\sqrt{3}$-Au surface system (see Chapter 5), has a surface energy which is close to that of models HCT-2. From the above discussion, we conclude that the HCT-1a is the energetically most favorable structural model for this surface. It will be referred to simply as HCT-1, when there is no confusion involved. Several recent experimental investigations [12, 21] have proposed models essentially identical to the theoretical HCT-1 structure. Our structural parameters are compared with those reported in RHEED and X-ray experiments in Table 4.3.

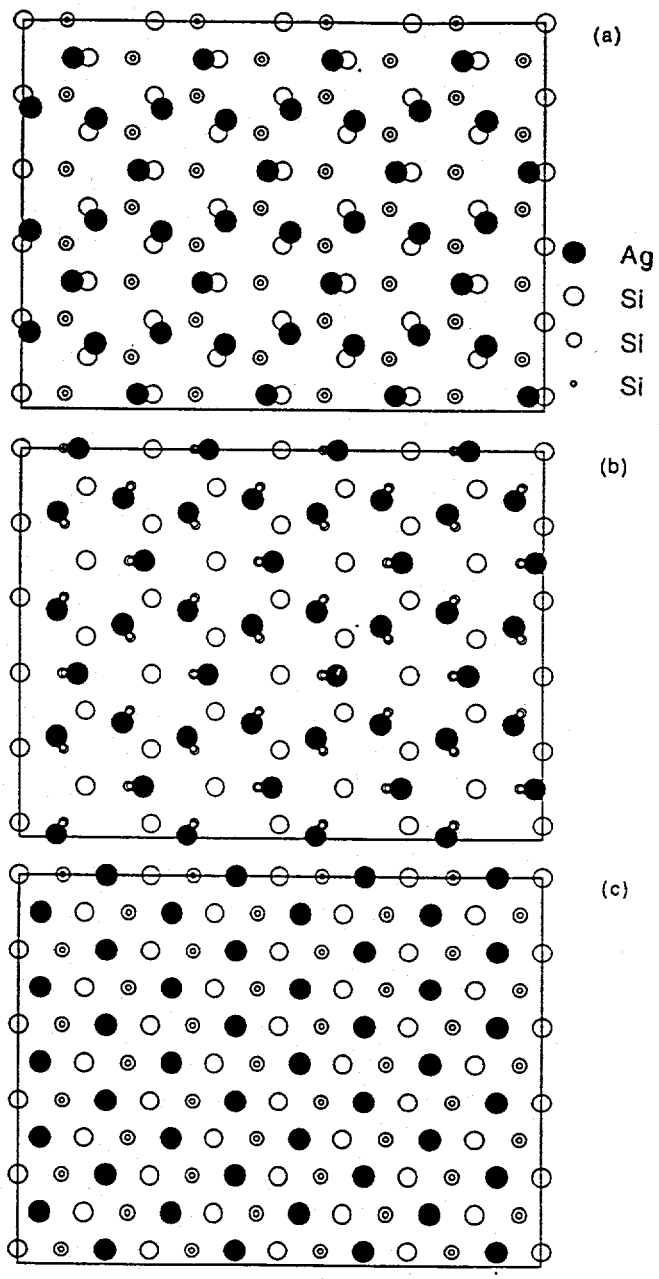

Figure 4.8: Variations of HCT-2 type models (top view). (a) HCT-2a; (b) HCT-2b; (c) HCT-2c.

Table 4.3: Comparison of the theoretical structural parameters of the lowest-energy HCT-1 model with experimental results. The z-Ag and z-Si are the vertical distance of the top Ag and MTL Si layers above the first Si double layer.

	RHEED [19]	X Ray [22]	X Ray [23]	HCT-1
d(Ag-Ag)	3.36	3.426	3.43	3.45
d(Ag-Si)		2.593	2.57	2.54
		2.596	2.63	2.60
d(Si-Si)	2.75	2.308	2.32	2.51
z-Ag	2.95	3.055	3.05 [24]	3.15
z-Si	2.2	2.259	2.26 [25]	2.30

As shown in Figure 4.6, the HCT-1 structure can be envisioned as follows: Start with a clean "missing top layer" Si (111) surface (i.e. each top layer atom has 3 dangling bonds). Put one monolayer of Ag above the 5th (or 6th) Si layer, so that it is 0.85 $\AA$ above the 1st Si layer and 3.15 $\AA$ above the 2nd Si layer (the first intact double layer). The Ag layer reconstructs, with lateral displacements characterized by a parameter x (see Figure 4.6 (a)) which is found to 0.43 a (a is the lattice parameter of the surface unit cell). After the reconstruction, the Ag-Ag has nearest neighbor (n.n.) distance of 3.45 $\AA$. The in-plane n.n. Si-Si distance in the top Si layer is substantially smaller than that on an ideal surface so that two of the three broken bond of the top Si layers are reformed by the Si trimers. The remaining dangling bond is satisfied by the Ag atoms. The n.n. Ag-Si distance is 2.54 $\AA$. The third Si layer has a buckling of about 0.2 $\AA$, with 2/3 of the atoms positioned above the other 1/3. We note that if we impose a (1×1) surface unit cell (lateral relaxation not allowed), one ML of Ag on top of an intact double layer Si surface actually has lower surface energy than the one with a MTL configuration. It is the substantial lateral reconstruction of the top layer Si atoms allowed in the MTL configuration that makes it more favorable in the $(\sqrt{3} \times \sqrt{3})$ unit cell.

STM Image and Electronic Density of States

Since the atoms in the top Ag layer are not arranged in a honeycomb structure, our model has to be reconciled with the observed STM images. Since the STM images are governed by the spatial distribution electronic states involved in the tunnelling process [125], we examined the wavefunctions of electronic states in the energy range from -2.5 eV to 2.0 eV around the Fermi level ($E_f = 0$ eV). We found that the

charge distributions for the occupied states (-2.5 eV to 0 eV) resemble the atomic honeycomb-chained-trimer arrangement. Above the Fermi level, from 0 eV to 1 eV, the electron charge distribution is dominated by a band of empty surface states. Figure 4.9 shows a charge density plot of the states from 0 to 1 eV in a plane parallel to and 1.5$\mathring{A}$ above the top Ag layer. The plots exhibit the honeycomb pattern observed by STM. This result is consistent with the bias-voltage dependence of the STM images: the best resolved honeycomb images were obtained for bias conditions where the electrons are tunnelling from the tip into the empty states which we will show in the next section are from a surface band. We also observe from Figure 4.9 that the maxima of the electronic distribution for the empty states occur at the center of the Ag trimers and are situated over the fourth Si layer, in agreement with the registry determined by Wilson and Chiang [40].

Figure 4.10 shows the electronic densities of states (DOS) of the slab for several structural models including the HCT-1 model. The DOS are obtained from the eigenvalues of 37 evenly spaced **k** points in the IBZ with a Gaussian smearing of 0.2 eV. We have tested the results with different numbers of **k** points. DOS computed with 16, 37 and 70 **k** points show little change. We notice in the result for the HCT-1 model that the Fermi level E_f is located near the bottom of a "pseudo-gap": a region of about 1 eV wide where the DOS drops to a very low value. HCT-1 is the only class of model we have studied that gives something close to a gap in the DOS near E_f. Earlier photoemission experiments have reported a gap for the $(\sqrt{3} \times \sqrt{3})$ surface. It is possible that the small density of states in the pseudogap region could have escaped detection in those experiments. However, surface charging effects may also be important for the interpretation of the photoemission data. Quantitative

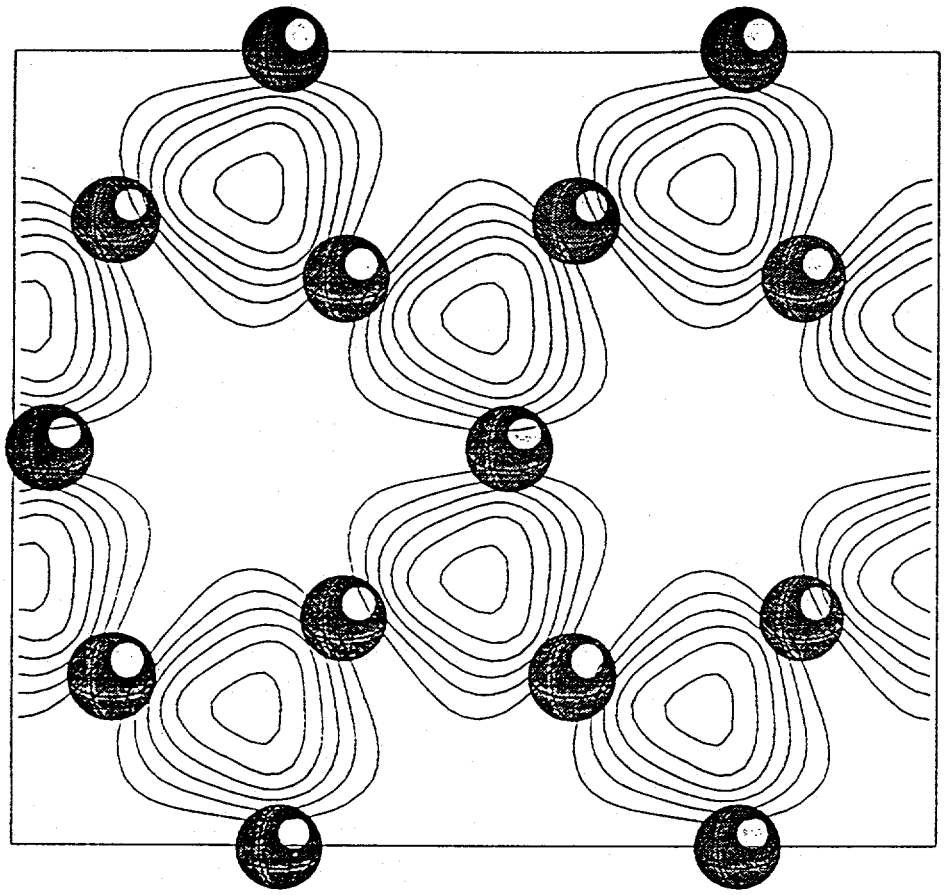

Figure 4.9: Electronic charge-density plot for unoccupied surface states on a horizontal plane 1.5 $\AA$ above the top Ag Layer. Calculated results of HCT-1 model. The black dots mark the position of the Ag atoms.

comparison between our results and photoemission and STM experiments will have to include the effects of surface charging [36] and surface band-bending, as well as the shift of energy position of the surface band relative to the bulk states as the surface becomes charged.

Surface States

We have seen that those states in the gap range of about 1 eV wide above the Fermi level form the honeycomb shape STM image, we are thus motivated to calculate the surface band structure of the $\sqrt{3}$-Ag surface. For better and easier identification of the surface states or resonances, we increase the slab thickness from six to eight layers in the HCT-1 model. The iteration are continued until the atoms in the configuration are fully relaxed by using the Hellmann-Feynman force calculation. The self-consistent potentials are obtained by iterating with 7 k-points in the irreducible SBZ. After reaching self-consistency, the electronic band structures of the systems are calculated along the symmetry directions $\bar{\Gamma} - \bar{K} - \bar{M}$. To facilitate the identification of the surface states, we also calculate the projected band structure for the Si(111) surface. This is done by projecting the bulk band structure of Si on to the two dimensional (111)-SBZ. Results are shown in Figure 4.11 where the zero of the energy corresponds to the Fermi energy. For the HCT-1 model, the Hamiltonian matrix have reflection symmetry (see Figure 4.6) about the plane perpendicular to the (111) surface that passes along the $\bar{\Gamma} - \bar{M}$ line. For such reflection symmetry, the electronic states with wave-vectors along these symmetry lines can be separated into two groups with even and odd symmetries, and they are represented in Figure 4.11 by dashed and solid lines.

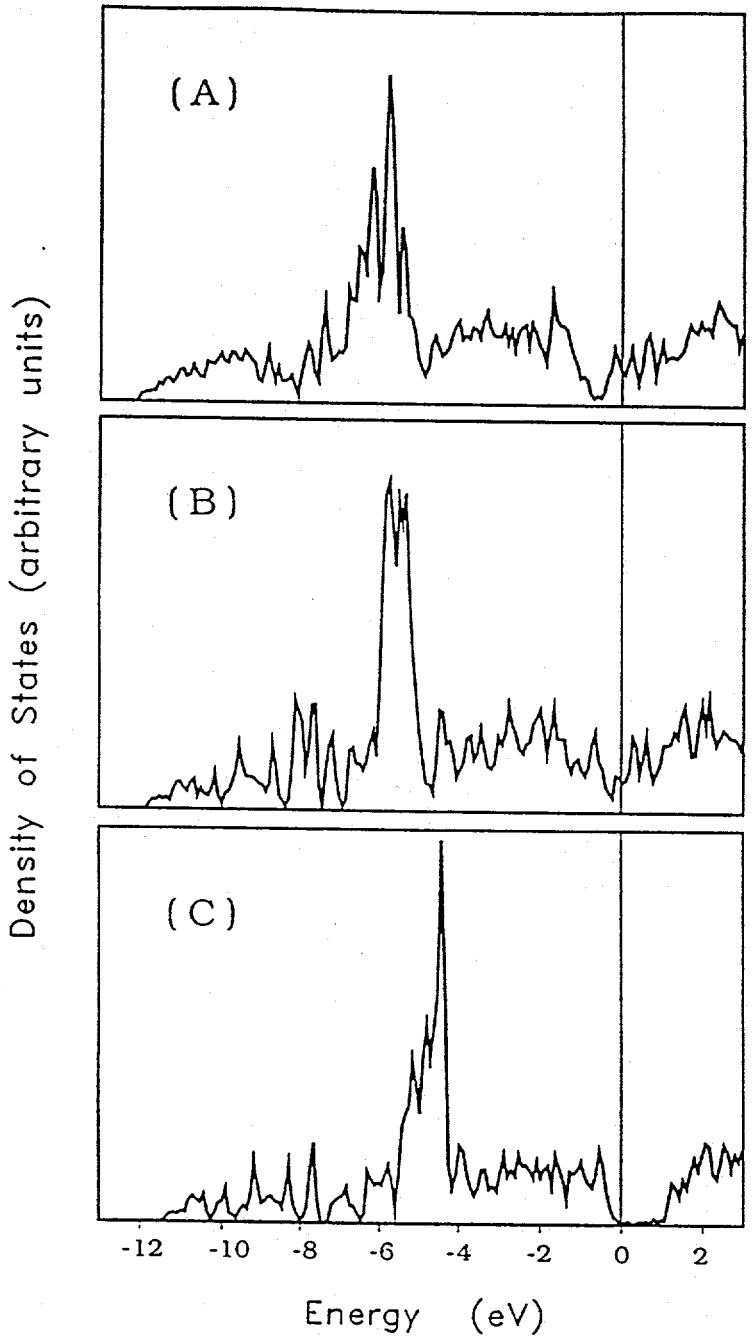

Figure 4.10: Electronic density of states (DOS) for different models: (a) ET; (b) ST; (c) HCT-1.

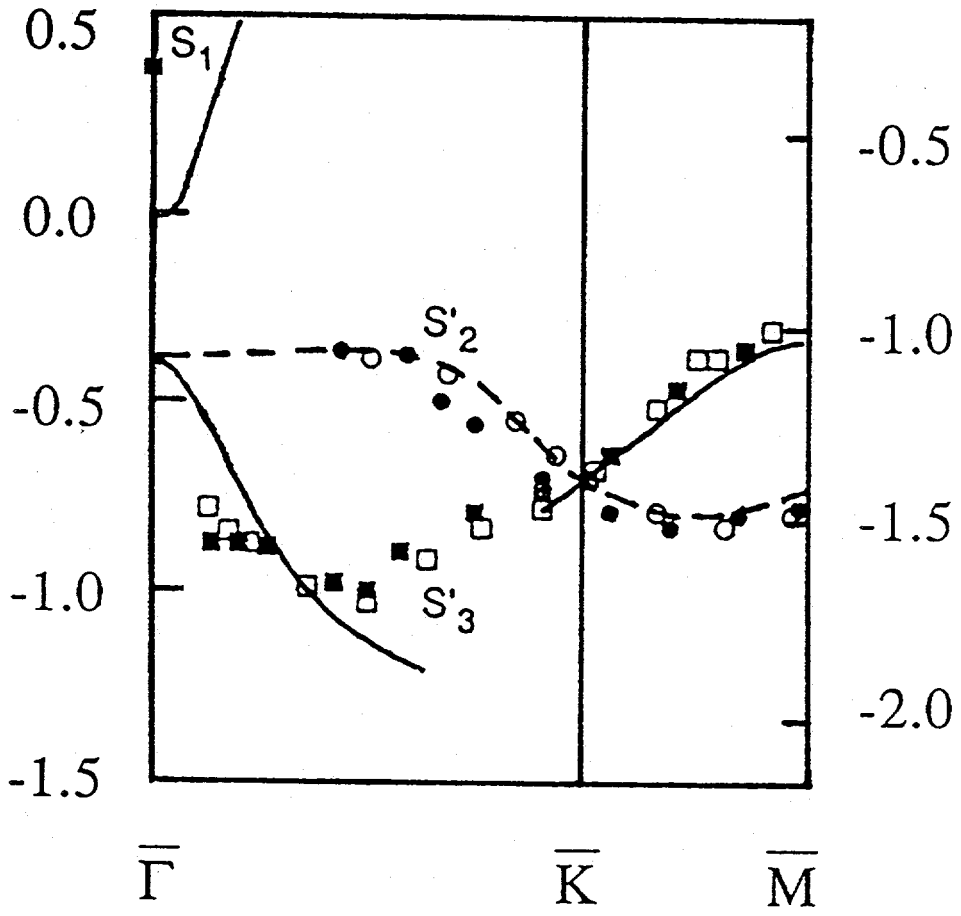

Figure 4.11: Surface states and resonances in the $\bar{\Gamma} - \bar{K} - \bar{M}$ direction. Dashed and solid lines are theoretical results for even and odd states respectively; Open and filled circles and squares are experimental results taken from Fig.4 in Ref. [37]. The Fermi level is set at 0 eV for both theory (left axis) and experiment (right axis).

Several criteria guided us to locate the surface states and resonances in the surface band structure. Surface states usually appear as extra energy levels in the gaps of the projected bulk bands, and since a slab geometry has two surfaces, they usually occur in almost degenerate pairs (slightly split by the interaction of the surface states). The key criterion we used is to look for states with wavefunction amplitudes (representing charge density) highly localized (more than 50%) within the first one or two layers of the surface according to the degree of localization at the surface.

Displayed in Figure 4.11 as dashed or solid lines are states with charge localized mainly on the Ag layer. It is clear that the states in the energy region of about 1 eV above the Fermi level comes from a surface band (S_1) whose minimum is located at the center of SBZ. This band overlaps with the valence band top at the center of the surface Brillouin zone by less than $\sim$0.1eV, and then rises sharply with increasing $\vec{k}$ away from the zone center giving rise to the very low value of DOS in this region. The charge density contours plotted in Figure 4.9 are in fact from this surface band with its charge localized above the Ag layer, which has been observed in STM experiment.

This surface state has been observed by Johansson, Landemark, Karlsson and Uhrberg [37] in their polarization-dependent angle-resolved photoemission experiment. They clearly established that the $(\sqrt{3}\times\sqrt{3})$ surface has a mirror plane containing the surface normal and the $[11\bar{2}]$ direction, a threefold symmetry of the surface, and existence of a highly dispersive surface state (S_1) with its minimum close to the Fermi level at the $\bar{\Gamma}$ point in SBZ. These observations offer strong support for the HCT-1 model that we have found for the $\sqrt{3}$-Ag surface. The HCT-1 model, shown in Figure 4.6, does have the mirror plane, a three-fold rotational symmetry, and the S_1 surface state, as found in the experiment. The existence of this surface band gives

a natural explanation to the big band bending shift upon formation of the $\sqrt{3}$-Ag surface and the pinning of the Fermi level close to the valence band top [37].

In addition, the HCT-1 model also has other surface resonances besides the S_1 surface states that matches well with the photoemission data [37]. We show in Figure 4.11 surface states and resonances in the $\bar{\Gamma} - \bar{K} - \bar{M}$ direction, within about 2 eV of the valence band maximum, and compared with the surface states observed in the photoemission experiment. Surface states in this direction are either even or odd with respect to reflection of the mirror plane mentioned above, and they are marked by dashed and solid lines respectively. Since the S_2' states are found to be even and S_3' states to be odd in the photoemission experiment, the dispersion and the symmetry properties of these states have good agreement between theory and experiment, lending further support for the HCT-1 model. Due to surface band-bending and surface charging effects, and also the reported time dependence of the Fermi level position, it is difficult to compare the absolute position of the surface states. Hence, for comparison purposes, we have aligned the theoretical and experimental surface band structures at the energy where the S_2' and S_3' states cross each other. We note that in the HCT-1 model, the S_2' and S_3' states cross each other at 0.72 eV below the bottom of the S_1 surface state in our calculation, whereas in the experiment, it is about 1.0 eV below the bottom of the S_1 state. We also note that in our model, the bottom of the S_1 surface state is slightly (less than 0.1 eV) below the valence band maximum (VBM), whereas in the experiment, it is 0.1 eV above the VBM for a new surface and 0.1 eV below VBM for an old surface. A self-consistent LCAO-$X\alpha$ band structure calculation [68] with a six layer slab based on structural coordinates determined from a coaxial impact-collision ion scattering

spectroscopy and energy minimization using the Keating model [12] found a gap of 0.54 eV for this system. The slab we employed in our first principles calculations contains eight layers of Si, which is thick enough for the determination of surface atomic arrangements but it is desirable to have thicker slabs for an unambiguous identification of surface resonances.

Summary

In summary, we have used first principles calculations to determine the structure of the $\sqrt{3}$-Ag surface. Many plausible models have been tested. Our calculations show that the energetically most favorable structures for the $\sqrt{3} - Ag$ surfaces is the 1 ML coverage HCT-1 model. This is the only model structure with surface energy that wets the Si surface. It gives a pseudo-gap which explains the photoemmision experimental results. This model also has electronic properties that are consistent with the observed STM images.

CHAPTER 5. STUDY OF THE SURFACE STRUCTURE OF $(\sqrt{3} \times \sqrt{3})$ $R30^\circ$ Au/Si(111)

Introduction

With detailed studies of the geometry of the $(\sqrt{3} \times \sqrt{3})$ $R30^\circ$ Ag/Si(111) surface [66, 67], we have obtained unambiguously a ground state atomic arrangement (see Chapter 4), which agrees with experimental evidence from X-ray diffraction [20-24], photoelectron diffraction [31], and ion-scattering experiments [3-12]. An interesting twist in the ground state structure is that, unlike most of the proposed models, the top layer atoms do not form a honeycomb structure. The honeycomb pattern observed in scanning tunneling microscopy (STM) experiments [39, 40] is shown from our calculations to arise from the electronic charge density of an empty surface band near the Fermi level and does not represent the positions of the atoms in the top layer. Motivated by the chemical similarity of Ag and Au, we extend our calculations to investigate the corresponding $(\sqrt{3} \times \sqrt{3})$ $R30^\circ$ Au/Si(111) surface (hereafter referred to as $\sqrt{3}$-Au surface).

Surprisingly, STM studies performed on the $\sqrt{3}$-Au surface [48-51] revealed images which are qualitatively different from the $\sqrt{3}$-Ag surface: the STM images display only one bright spot per $\sqrt{3} \times \sqrt{3}$ unit cell instead of two bright spots for the honeycomb pattern observed on the Ag adsorbed surface [39, 40]. However, Chester

and Gustaffson [47] suggested from ion-scattering experiments that the geometry of $\sqrt{3}$-Au surface is closely related to the ground state structure for the $\sqrt{3}$-Ag surface. The missing top layer twisted trimer models (MTLTT) [47] proposed in their paper differ from the ground-state $\sqrt{3}$-Ag geometry only by an additional rotation of the top layer Ag and Si atoms about the three-fold axes. In other ion-scattering experiments, Oura et al proposed a competing modified triplet coplanar model (MTC) [45] while Huang and Williams proposed a model consisting of a mixture of simple honeycomb and centered hexagons (HCH) [46]. Many other experimental techniques have also been used to study this surface system [54-61].

In this chapter, we present calculated results for the surface structure of the $\sqrt{3}$-Au surface and compare the ground state geometry with that of the $\sqrt{3}$-Ag surface. The lowest energy geometry obtained from our first principles calculations is consistent with available experimental data; in particular, the observed STM images are accurately reproduced.

First-principles Calculations

We have performed first-principles total energy calculations for many proposed structural models for the $\sqrt{3}$-Au surface. The calculations were performed within the local density functional formalism [115] using the Wigner [116] form of local exchange-correlation potential. Norm-conserving pseudopotentials [77] are used to represent the interactions between the valence electrons and the ion-cores and, in the electronic structure calculations, the Bloch wavefunctions are expanded in a mixed basis set [119, 120] comprised of both plane waves (with a 10.5 Ry cutoff) and numerical orbitals centered at the Au atomic sites. The optimized values for α and r_c are 0.70

and 2.70 a.u., respectively. For each structural model we have tested, a "supercell" geometry (equivalent in thickness to 12 Si layers in the $< 111 >$ direction) is used to model the surface system. There are 6 layers of Si beneath the Au layer. For models in which the Au layer is in an embedded geometry, an additional Si layer is put above the Au layer. Self-consistency is obtained with seven **k**-points in the 2-dimensional irreducible Brillouin zone. All atoms are allowed to relax both laterally and vertically (within the symmetry constraints imposed by the individual models) according to the calculated Hellmann-Feynman forces until the zero-force equilibrium positions are obtained. In some cases, several starting configurations are tested to avoid the possibility of being trapped in local energy minima.

Structural Models

All the experimentally proposed models for the $\sqrt{3}$-Au surface have a nominal Au coverage of 1 ML [47, 45], (or close to 1 ML, as in HCH [46]). Our previous calculation for $\sqrt{3}$-Ag surface indicated that the most energetically favorable structure for the $\sqrt{3}$-Ag surface (the HCT-1 model) [67] also has 1 ML Ag coverage. Therefore in the present work, we have focused our attention on geometries with 1 ML Au coverage. The models we have investigated are listed in Table 5.1. They can be classified into two groups by the stoichiometry of the first Si layer: (1) models with one Si vacancy per $\sqrt{3}$ surface unit cell in the first Si layer and the Au atoms are either on top (MTC model [45]) or embedded (a conjugate missing layer model (CMTL) and embedded trimer (ET) model [39]); (2) models with no vacancy for the first Si layer which is beneath a layer of Au atoms on the top: MTLTT model [47], HCT-1 model [67] and a conjugate HCT-1 (CHCT-1) model (see Figure 5.1).

Table 5.1: Lists of structural models and their surface energies. The Si vacancy is in unit of ML, and the surface energy in unit of J/m^2. (1 J/m^2 = 2.4 eV per $\sqrt{3} \times \sqrt{3}$ surface unit cell.)

Models	Top Si vacancy	Ag position	Surface Energy
ET (MTC)	1/3	embedded	2.487
CMTL	1/3	on top	1.292
HCT-1	0	on top	0.844
CHCT-1 (MTLTT)	0	on top	0.402
CHCT-2	0	on top	0.478

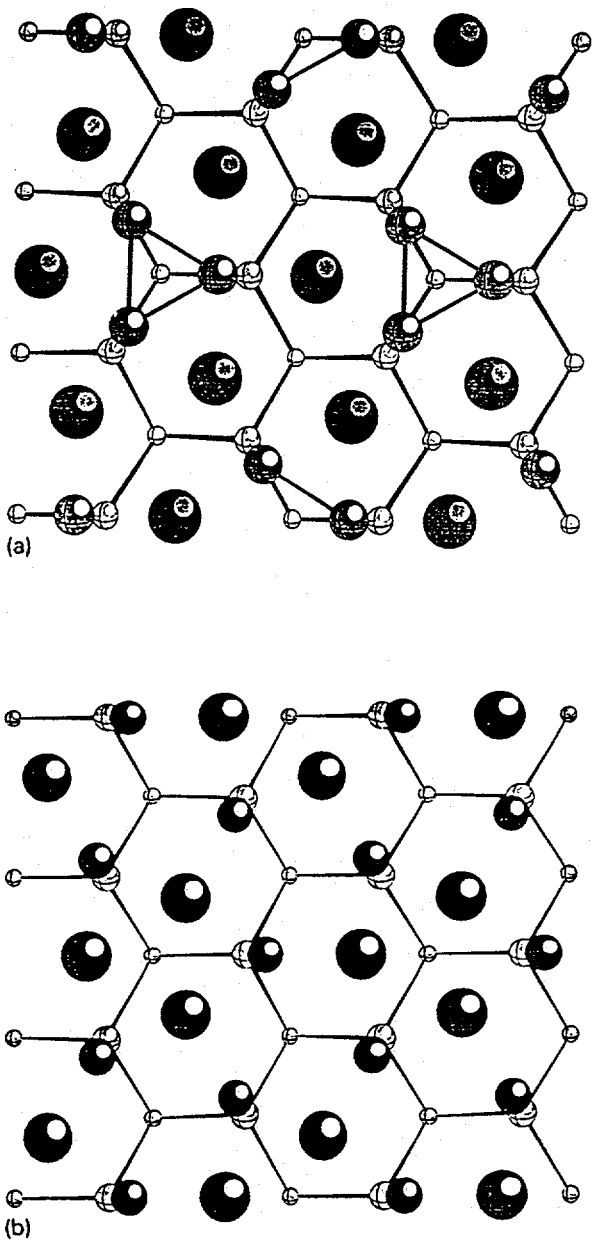

Figure 5.1: Comparison of (a) HCT-1 and (b) CHCT-1 models. The largest dots are Au atoms. The rest are Si atoms from three layers, with sizes decreasing from the surface to deeper layers.

The CMTL model is related to the MTL model [19] proposed by several authors for the $\sqrt{3}$-Ag surface, by having the Au and first layer Si atoms interchanged so that the Au coverage is 1 ML. The MTC model could be viewed as a variant of the ET model. The difference between them is only whether the Au layer is embedded below or situated above the first Si layer. In our calculation, we find that the MTC model is energetically much less favorable than the ET model. Au trimers initially put on top of the Si substrate always relax downward and become embedded, resulting in the ET structure.

For the second group of models, we start from the same initial structure: 1 ML Au atoms sitting on top of a "missing top layer" (MTL) Si substrate, with Au atoms positioned above the 5th layer Si atoms. If the first layer Si atoms cluster around the third layer Si sites to form isolated trimers, while the top layer Au atoms relax away from the third layer Si sites to form a network of "honeycomb-chained-trimers," as depicted in Figure 5.1 (a), the resulting configuration is the so-called "HCT-1" model. Alternatively, the Au atoms can cluster around the third layer Si sites to form trimers while the Si atoms form an array of honeycomb-chained-trimers, as shown in Figure 5.1 (b). Since this structure is just the "conjugate" of the HCT-1 model, we call it the "CHCT-1" model. Thus both models can be obtained by the superposition of two ordered arrays, one of Si trimers and the other of Au trimers, both centered about the third layer Si atoms, respectively. If we allow these Au and Si trimers to rotate freely about the three-fold axes through the third layer Si atomic sites, while also allowing the trimers to contract, we can obtain a series of intermediate structures of lower symmetries that allow the surface to vary continuously between the HCT-1 and the CHCT-1 models. The structures 1 and 2 of the MTLTT model can be generated

in this manner (see Figure 5.2). In our calculation, we find that these intermediate structures are less stable than the CHCT-1 structure. We have tested the MTLTT structures explicitly by using the suggested parameters as starting configurations. After relaxation, both structures relax back to the CHCT-1 structure. Actually, For any initial rotational angles we have tested, the surface always relaxes itself to the CHCT-1 structure, which has higher symmetry and is more stable.

The relative stability of different models can be obtained by comparing the surface energy per $(\sqrt{3} \times \sqrt{3})$ unit cell of the composite Au/Si system: it is defined as $\frac{1}{2}(E_{tot} - N_{Au}E_{Au} - N_{Si}E_{Si})$, where E_{tot} is the total energy of the slab, N_{Au} and N_{Si} are the number of Au and Si atoms in the slab respectively, and E_{Au} and E_{Si} are the total energy per atom of bulk Au and Si. The factor $\frac{1}{2}$ is because there are two surfaces in a slab. The surface energy results from our calculation are listed in Table 5.1. In decreasing order of surface energy, the models we have tested can be listed as follows: the CMTL model, the ET model, the HCT-1 model, and the CHCT-1 model. A schematic surface energy diagram is shown in Figure 5.3. For the CHCT-1 model, the energies for 2 possible registries of Au are shown.

Due to the use of the local density approximation, it is difficult to estimate the absolute error in the surface energy. For different geometries that are calculated with the same basis set, k-point sampling, and slab and vacuum thickness, we estimate that the relative surface energies can be trusted to about 0.1 J/m^2. It is therefore quite certain that within the limitation of the LDA, CHCT-1 is the most energetically favored model within the class of models we have considered. It should be noted, however, that within the same class of models, the surface energy difference between different registries of the Au atoms is close to the uncertainty of the calculations.

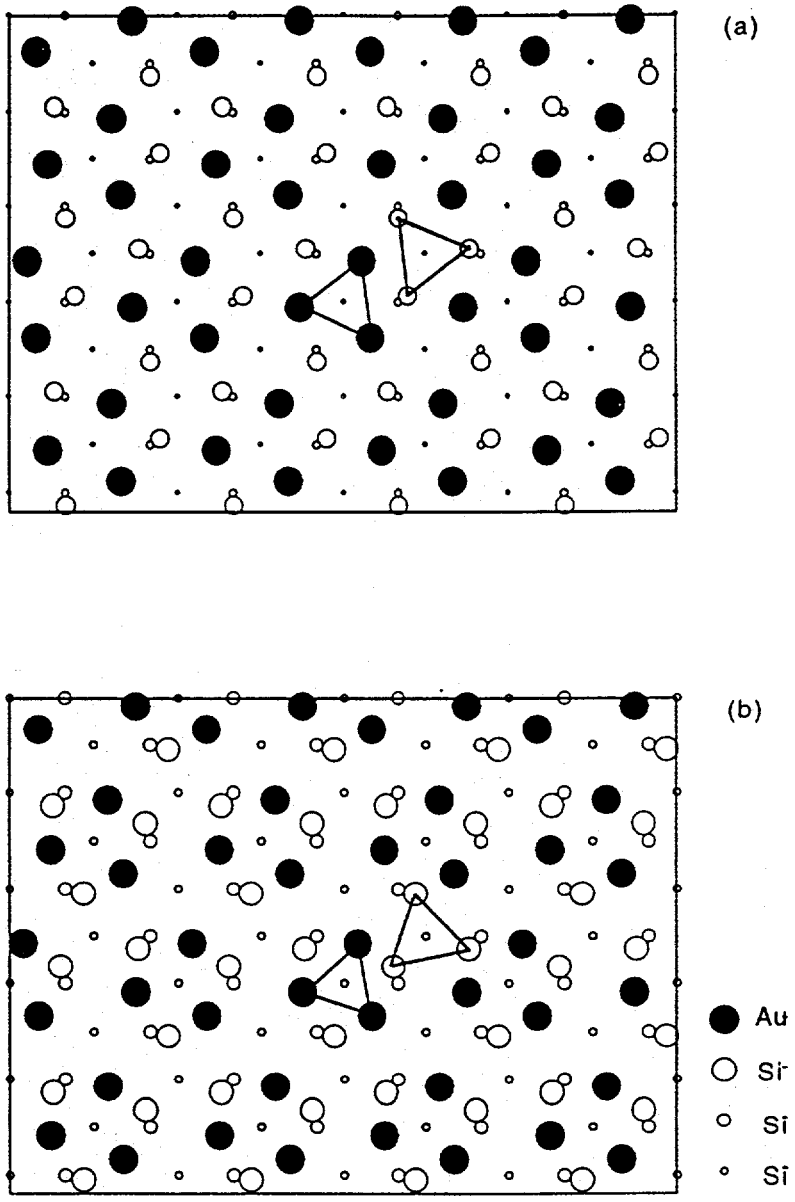

Figure 5.2: Top view of the structural model MTLTT [47]. Note the different rotational directions. (a) Both Au and Si trimers rotate counter-clockwise (C.C.W.); (b) Au: C.C.W.; Si: C.W.

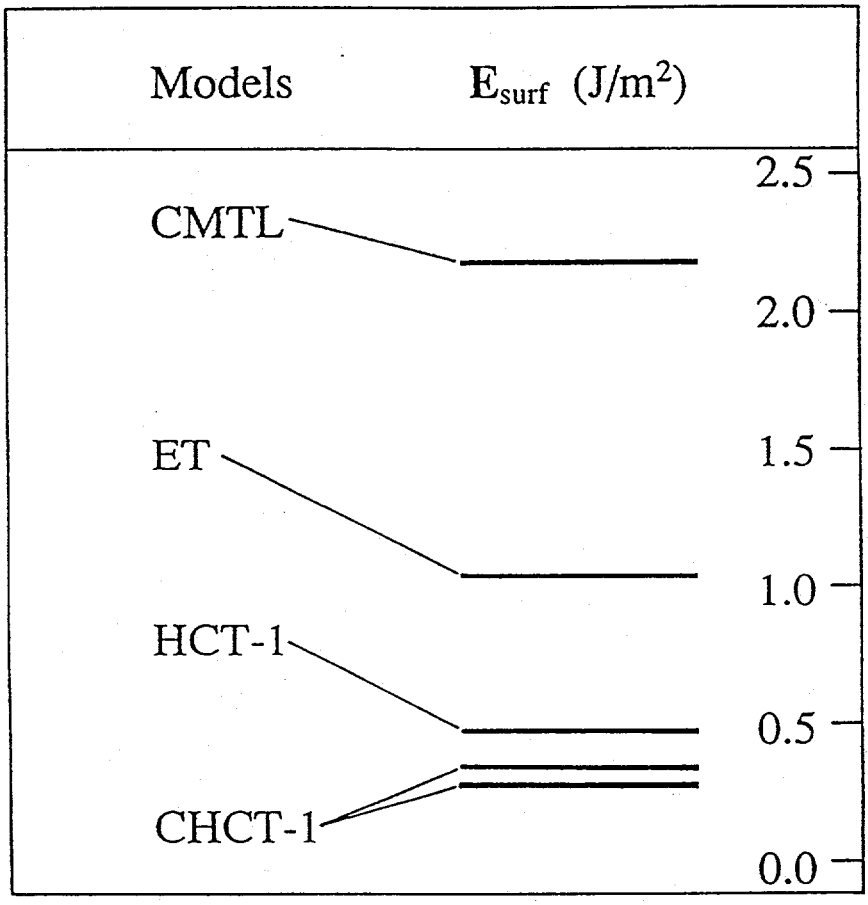

Figure 5.3: Schematic surface energy diagram for a few models of Au/Si(111). For comparison, the surface energy of clean Si(111) (2×1) is about 1.24 J/m^2 [123].

The ground state configuration of the CHCT-1 model for the $\sqrt{3}$-Au surface also has a surface energy lower than that of reconstructed clean Si(111) surface, which assures that the Au atoms wet the Si(111) surface. The fact that the surface energy of the CHCT-1 structure is even lower than that of the HCT-1 structure indicates that strong Au-Au bonding is the dominant factor determining the structure of the $\sqrt{3}$-Au surface.

As shown schematically in Figure 5.1, the structure of the CHCT-1 model could be viewed as obtained from the HCT-1 model by reversing the lateral relaxation directions of the Au and top Si atoms, while keeping the Au atoms as the topmost layer. As a result, the Au atoms form isolated trimers, while the first layer Si atoms take the honeycomb-chained-trimer arrangement. The Au trimers are centered above the third layer Si atoms, giving the surface threefold symmetry which has been reported from experimental observations [60]. In the ground state configuration, the Au trimers have a nearest neighbor (n.n.) distance of 2.83 $\AA$. The Au layer is positioned 0.56 $\AA$ above the first Si layer, 2.92 $\AA$ above the second Si layer and 3.74 $\AA$ above the third Si layer. The in-plane n.n. distance for Si top layer atoms is 3.50 $\AA$, just slightly smaller than that of Si on an ideally truncated surface (3.86$\AA$). The interplanar n.n. Au-Si bond length is 2.45 $\AA$. In Table 5.2, structural parameters of our theoretical CHCT-1 model are compared with those of experimental models for the $\sqrt{3}$-Au surface.

For the CHCT model, we have tested different registries. In CHCT-1, the Au atoms sit above the 5th layer Si atoms, while in CHCT-2 the Au atoms are above the 3rd Si layer (see Figure 5.4). In Table 5.1, we see that CHCT-2 has a slightly higher surface energy.

Table 5.2: Comparison of structural parameters of our theoretical model CHCT-1 and experimental data. d's are bond lengths between nearest neighbor atoms in the Au and first Si layers. z is the vertical distance between Au and Si layers. All values are in $\AA$.

	ICISS [45]	ICISS [46]	MEIS [47]	XRD [53]	LEED [56]	CHCT-1
d(Au-Au)	2.9	3.84	3.0/2.9	2.80	2.80	2.83
d(Au-Si)	2.53	2.8	2.6/2.8		2.416	2.45
					2.404	2.38
d(Si-Si)	3.84		3.2/3.2		3.50	3.50
z(Au-Si)	0.3	0.7-2.0	1.6/1.8		0.56	0.56

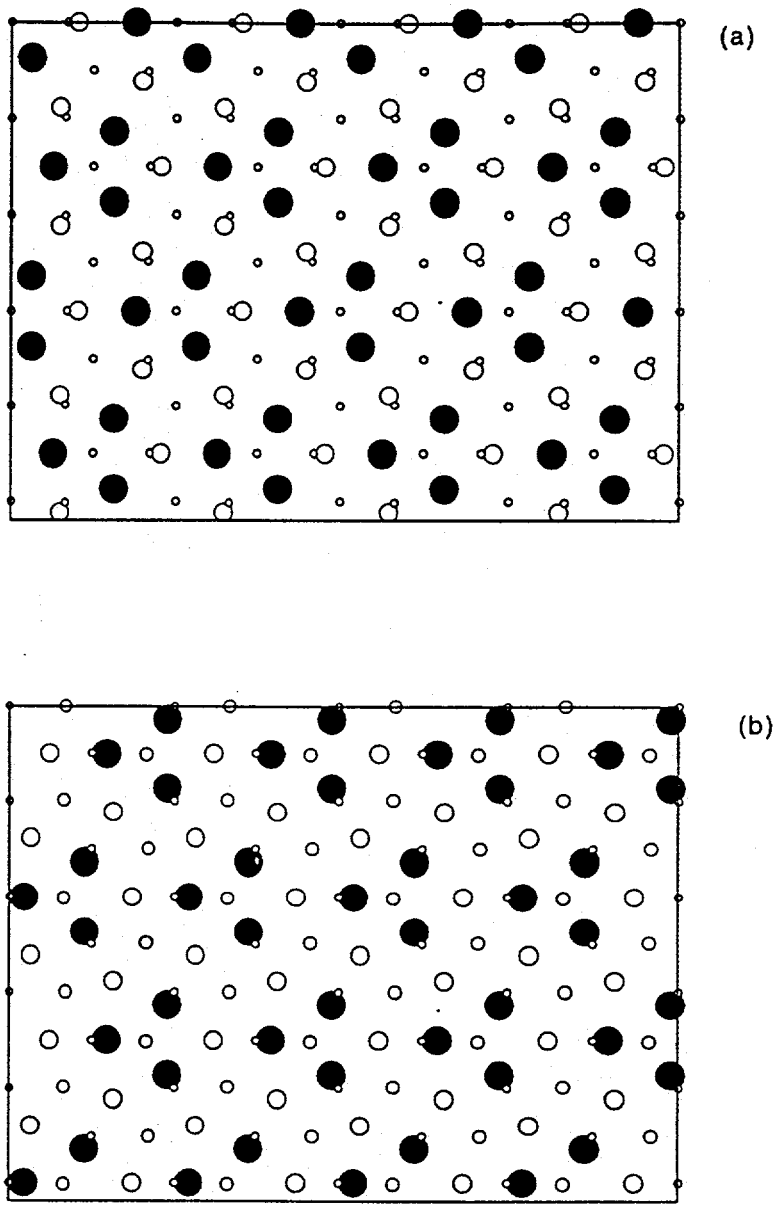

Figure 5.4: Top view of the structural models for the $\sqrt{3}$-Au surface: (a) CHCT-1; (b) CHCT-2;

Comparison of the $\sqrt{3}$-Au and $\sqrt{3}$-Ag Surfaces

Comparing our results for the $\sqrt{3}$-Ag and $\sqrt{3}$-Au surfaces, we note that the different atomic geometric structures can be accounted for by the difference in the binding energies of Au and Ag relative to that of Si. In the $\sqrt{3}$-Ag case, both the Ag-Ag and Ag-Si bonds are weaker relative to the Si-Si bonds. The primary process of reconstruction thus involves the rebonding of surface Si atoms to form trimers, and the Si layer reconstruction forces the Ag atoms into an array of "honeycomb-chained-trimers." Two of the three Si dangling bonds (in the distorted missing-top-layer configuration) can be satisfied by the trimer formation, with the remaining dangling bond satisfied by the Ag atoms. Au, on the other hand, has a higher cohesive energy than Ag (by ~0.9 eV/atom [134]). The Au-Si bond is also stronger than the Ag-Si bond. In this case, the Au-layer reconstructs to form a network of trimers, and the Si forms a network of HCT. In this configuration, the Au-Au n.n. distance (2.83 $\AA$) is much closer to that in bulk Au than it could be in a (1×1) situation.

The most significant difference in electronic properties between the $\sqrt{3}$-Ag and the $\sqrt{3}$-Au surfaces observed experimentally is the difference seen in STM images [39,40,48-51]. This could now be explained by the structural models we have obtained for $\sqrt{3}$-Ag and $\sqrt{3}$-Au surfaces respectively. By studying the properties of the electronic states for the $\sqrt{3}$-Au surface, we find that, similar to the case of the $\sqrt{3}$-Ag surface, the bright spots in the STM images are not the images of individual atoms, but rather reflect the patterns of the electronic charge from electronic states near the Fermi level. For states in the energy range from -2.0eV to +4.0eV (E_f=0eV), the charge density in a plane parallel to and above the Au layer of the $\sqrt{3}$-Au surface (as shown in Figure 5.5) gives a pattern that is similar to that observed by STM: one

"bright spot" in each $\sqrt{3}$ unit cell. The "bright spot" corresponds to a trimer of Au atoms and has a triangular shape quite similar to that observed in STM experiment [49]. We note that there is another subtle difference in the electronic behavior near E_f. For $\sqrt{3}$-Ag, we found that there exists an asymmetry between occupied and unoccupied states and only the unoccupied states give a clear "honeycomb" pattern with 2 "bright-spots" per unit cell; while for $\sqrt{3}$-Au, both the occupied and unoccupied states near E_f give the same hexagonal pattern (one "bright spot" per unit cell). This is in agreement with the bias-voltage dependences in the STM experiments for the $\sqrt{3}$-Ag and $\sqrt{3}$-Au surfaces [39, 40, 51]. However, the orientations of the triangular charge density spots for the $\sqrt{3}$-Au surface are different for the unoccupied states and the occupied states. In Figure 5.5, we can see that the pattern for the unoccupied states has triangular spots (Figure 5.5 (a)) with the same orientation as the Au trimers; for the occupied states, the triangles (Figure 5.5 (b)) are rotated by an angle of 30°.

We have also calculated the electronic density of states (DOS) of the surface for the CHCT-1 model structure. The DOS result is plotted in Figure 5.6. It is obtained from the eigenvalues of 16 evenly spaced k points in the irreducible Brillouin zone with a Gaussian smearing of 0.2 eV. The result shows no clear gap at the Fermi level. The position of the Fermi level (about 0.4 eV towards the valence band) suggests that the surface is metallic, which is in agreement with observations in photoemission experiment [55].

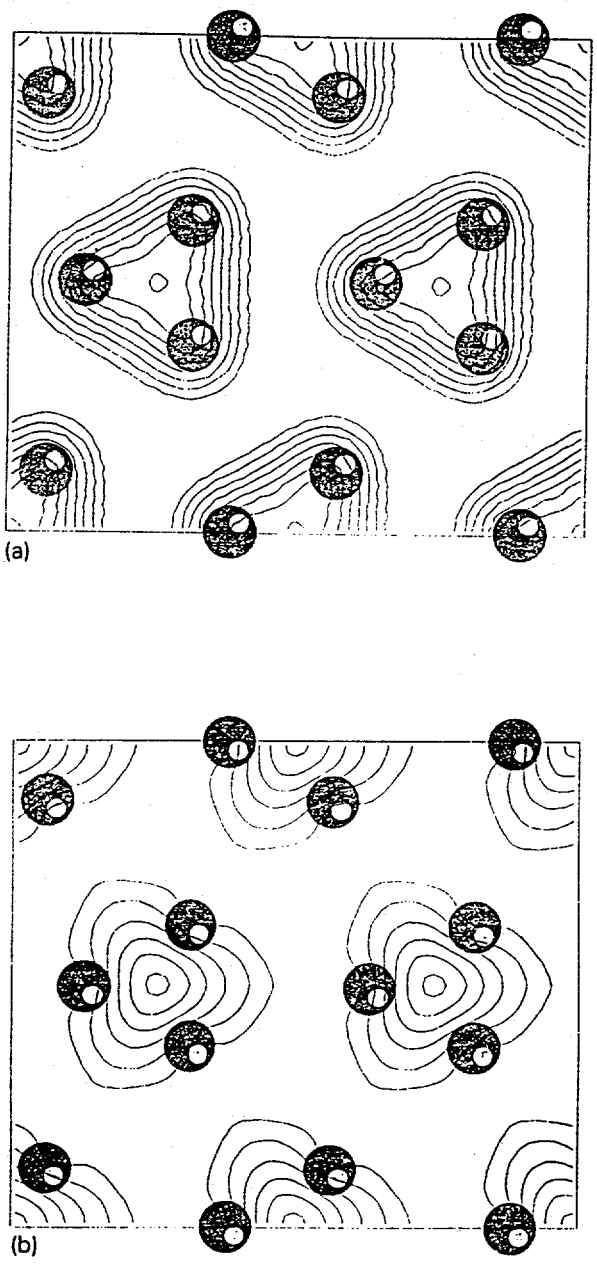

Figure 5.5: Contour plots of the electronic charge density for states around the Fermi level (E_f=0eV) in a plane 2.0 $\AA$ above the Au layer. (a). For unoccupied states in (0, 4eV); (b). For occupied states in (-2eV, 0).

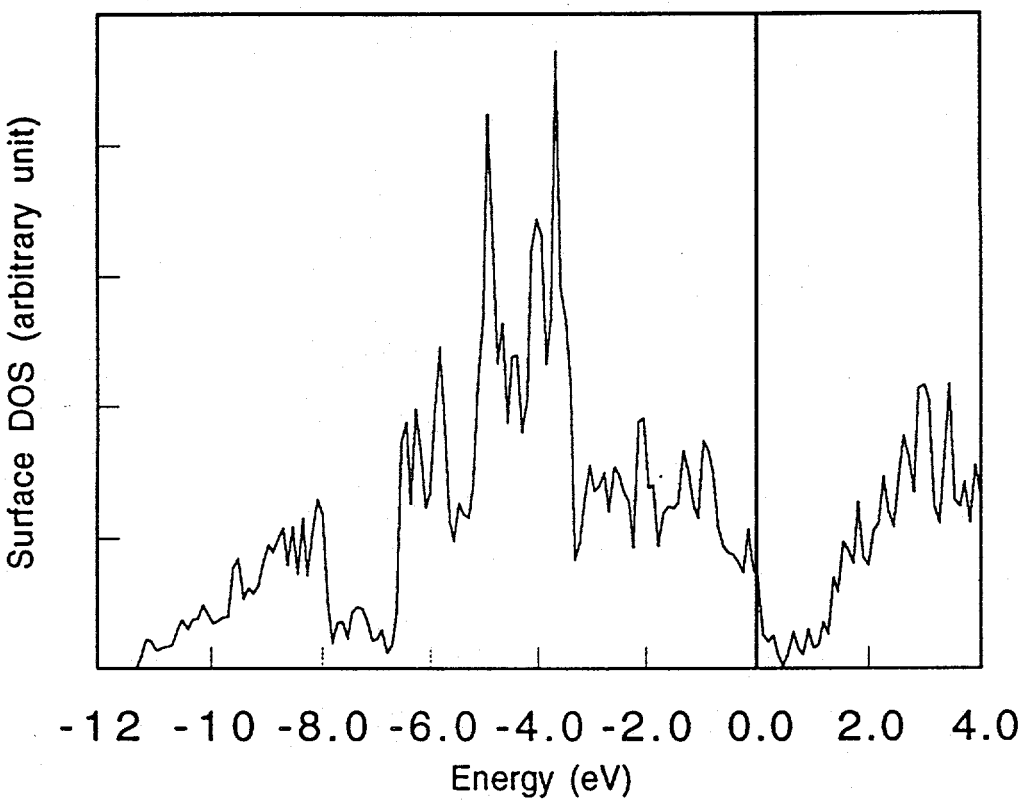

Figure 5.6: Electronic density of states (DOS) for CHCT-1 of the $\sqrt{3}$-Au surface.

Summary

In summary, we have used first principles calculations to determine the structure of the $\sqrt{3}$-Au surface. Most plausible models have been tested. Our calculation shows that the CHCT-1 model is the energetically most favorable structure. Among various models proposed by experiments, the models proposed by Chester and Gustafsson [47] is the closest to the CHCT-1 model This model also has electronic properties that are consistent with available experimental results.

CHAPTER 6. STUDY OF Ti-BASE BINARY SHAPE MEMORY ALLOYS

Introduction

Martensitic phase transition has been a hot topic for several decades due to the shape memory effect and many other peculiar properties present during the transition [106]. A lot of experimental and theoretical works have been devoted to the study of this phenomenon, yet many aspects of the transformation are still elusive. Ti based alloys are one member of this family that have attracted great interest in this field. In many Ti compounds, Martensitic transition occurs when they transform from the high temperature CsCl structure (B2) to the monoclinic primitive structure (B19′) or rhombohedral (R) structure during quenching. The transformation starts at Martensitic transformation temperature M_s and finishes at a lower temperature M_f. When some of these alloys are reheated, they can regain their original form, which has been known as shape memory effect. Recently, experiments have established some empirical correlation between the Martensitic temperature M_s and electronic properties of the alloys [106].

Using first principles method, we have performed total energy calculations and electronic structure analysis for a series of Ti based alloys in the B2 structure, the high temperature parent structure of these Martensitic alloys. For theoretical comparison,

we have done not only for the binary alloys TiFe, TiNi, TiPd, TiMo and TiAu which do exist, but also for Ti bcc metal and hypothetical B2-structured TiAl, TiAg and TiCu which are not found in nature. Our results reveal correlations between the Martensitic transformation temperature (M_s) and the electronic properties of these alloys.

The rest of the chapter is organized as follows: The first principles method is introduced in Section II. The optimization of the lattices of the alloys and the heat of formation results are discussed in Section III. The calculated density of states and the angular distribution of the electrons are presented in Section IV. The last section is a summary.

First Principles Method

In our calculations, norm-conserving ionic pseudopotentials [77] are used for the atomic cores. The total energies of the elemental metals and the alloys formed by these elements are calculated within the local density functional formalism [115] with the Hedin-Lundqvist form [114] of the local exchange-correlation energy. The electronic wave-functions are expanded by means of an efficient "mixed basis" set [119] consisting of plane waves with kinetic energy $(\mathbf{k}+\mathbf{G})^2$ up to a cutoff energy E_{cut} = 15.0 Ry and a set of localized Bloch functions centered at the atomic sites to describe the d-orbitals. Numerical functions are used for the radial part of the localized orbitals. The shape of the local orbitals are determined variationally from bulk calculations of the individual components of the alloy to optimize the convergence of the basis set. In this mixed basis scheme, the number of place waves needed for convergence is then reduced, leading to smaller Hamiltonian matrices and hence

less computation time. For the total energy calculations, 56 k-points are used in the irreducible Brillouin zone (IBZ). For the calculation of the electronic density of states (DOS), 256 k-points are used.

For optimized lattice constants, the electronic properties are analyzed by calculating the electronic density of states and angular momentum decomposition of the electron occupations.

Optimization of the Lattices

The bulk energy of the elemental metals are calculated first. The structures we employ is the ground state structures for the metals. The lattice constants are obtained by optimizing the total energy with respect to the volume. By comparing the total energy for the bulk with the atomic energy calculated by first principles with the same pseudopotentials, we obtain the cohesive energy. The experimental ground state configuration of the atoms are used in the atomic calculations. The results of optimized lattice constants and cohesive energy are shown in Table 6.1.

The lattice constants for the alloys in the B2 structure are then obtained. For each alloy, the total energy of the B2 structure is calculated for different volumes of the unit cell (Figure 6.1). A total energy versus volume curve is fitted, whose minimum gives the optimized lattice constants and the equilibrium total energy (see Figure 6.2). The curvature at the minimum gives the bulk modulus. The heat of formation for the alloy is the difference between the total energy of the alloy and the sum of the ground state bulk energies of the elemental metals. Results of the optimized lattice constants, total energy and cohesive energy for these alloys are listed in the Table 6.1. The results for those alloys that actually exist in B2 structure are plotted

Table 6.1: Results of the optimized lattice constants and bulk properties. Lattice constant a_0 is in Å, cohesive energy E and heat of formation H are in Ry per unit cell, and bulk modulus B_0 is in Mbar.

Element	Bulk Structure	a_0	E
Ti	hcp		-0.458
Al	fcc		-0.293
Mo	bcc		-0.493
Fe	bcc	3.379	-0.474
Ni	fcc	3.447	-0.377
Pd	fcc		-0.351
Au	fcc	4.118	-0.289
Ag	fcc	4.106	-0.206
Cu	fcc	4.397	-0.275

Alloy	a_0	H	B_0
Ti(bcc)	3.204	-.01795	1.240
TiAl	3.130	0.03755	1.207
TiMo	3.148	0.01997	1.918
TiFe	2.892	0.07518	2.581
TiNi	2.977	0.05066	1.853
TiPd	3.146	0.05952	1.717
TiAu	3.229	0.04097	1.724
TiAg	3.260	0.05047	1.224
TiCu	3.068	0.01081	1.432

in Figure 6.3 versus their experimental Martensitic transformation temperature M_s. From the figure, we see that corresponding to increasing M_s, the heat of formation decreases, lattice constant of B2 structure increases, and bulk modulus decreases. Smaller heats of formation, larger lattice constants, and smaller bulk modulus are consistent with a structurally weaker B2 phase, and thus consistent with a higher M_s (which means that the B2 phases are relatively less stable). The negative value of the heat of formation for Ti B2 structure indicates that the the hcp structure of Ti is energetically more favorable, which is in agreement with experiment.

Electronic Properties

The total density of states (DOS) are calculated for these alloys at their equilibrium volume. The results are show in Figures 6.4-6. The DOS are obtained from the eigenvalues of 256 k points in the IBZ with a Gaussian smearing of 0.2 eV. First of all, we focus on the positions of the Fermi level. For the most stable alloy TiFe, that is, the one with the lowest M_s, the Fermi level is located at the minimum of the DOS. When going to TiNi, TiPd, and TiAu, M_s becomes higher (the B2 structure becomes relatively less stable), the Fermi level shifts to the higher energy region and are situated on higher peaks. For TiMo, the Fermi level shift towards the lower energy side, and is also on a peak. For TiCu and TiAg that do not exist in B2 structure, the Fermi levels are at sharp high peaks of the DOS. From this, we see the correlation between M_s and the position of Fermi level.

We note that in the series TiMo, TiFe, TiNi, TiPd, and TiAu, the number of valence electrons in the second alloying element Fe, Ni, Pd, and Au increases. Roughly speaking, the DOS for these alloys have a generic twin peak structure and

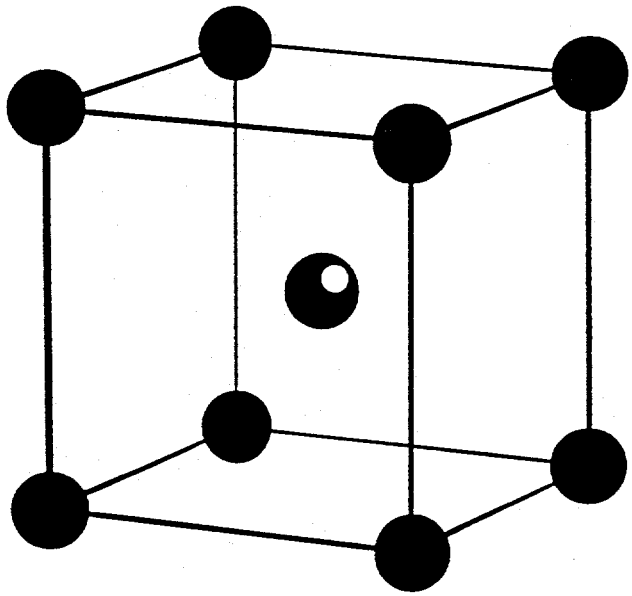

Figure 6.1: Unit cell of B2 (CsCl) structure, where one kind of atoms sit at the center and the second kind of atoms at the corners.

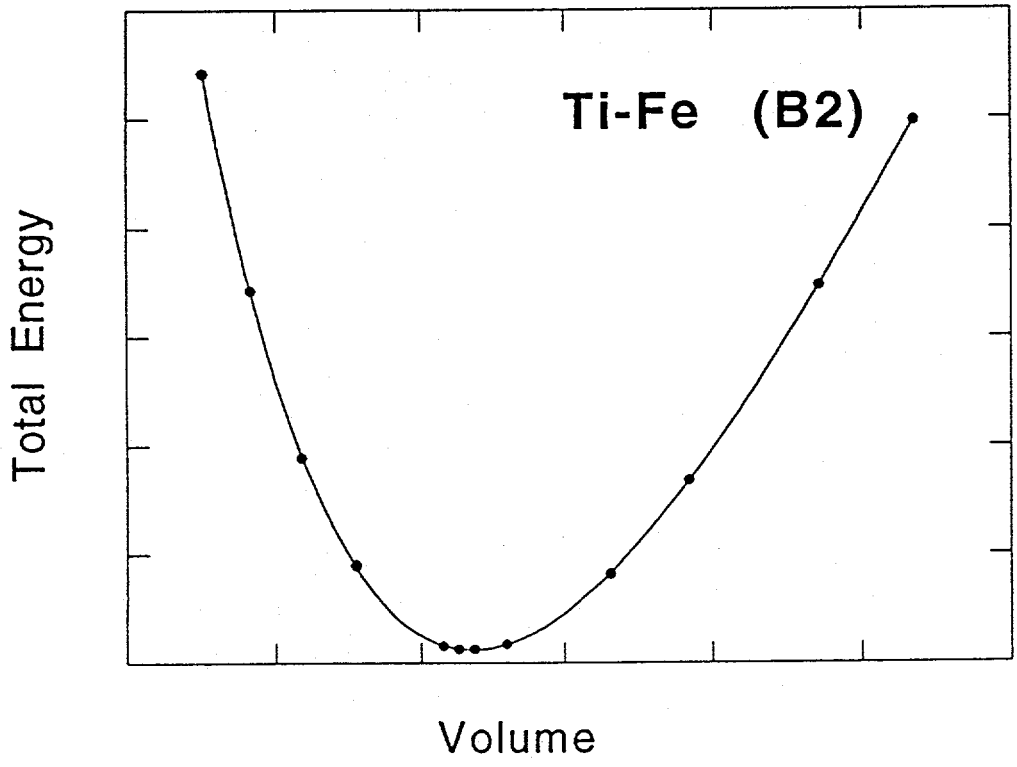

Figure 6.2: Theoretical curve of total energy vs unit cell volume for Ti-Fe.

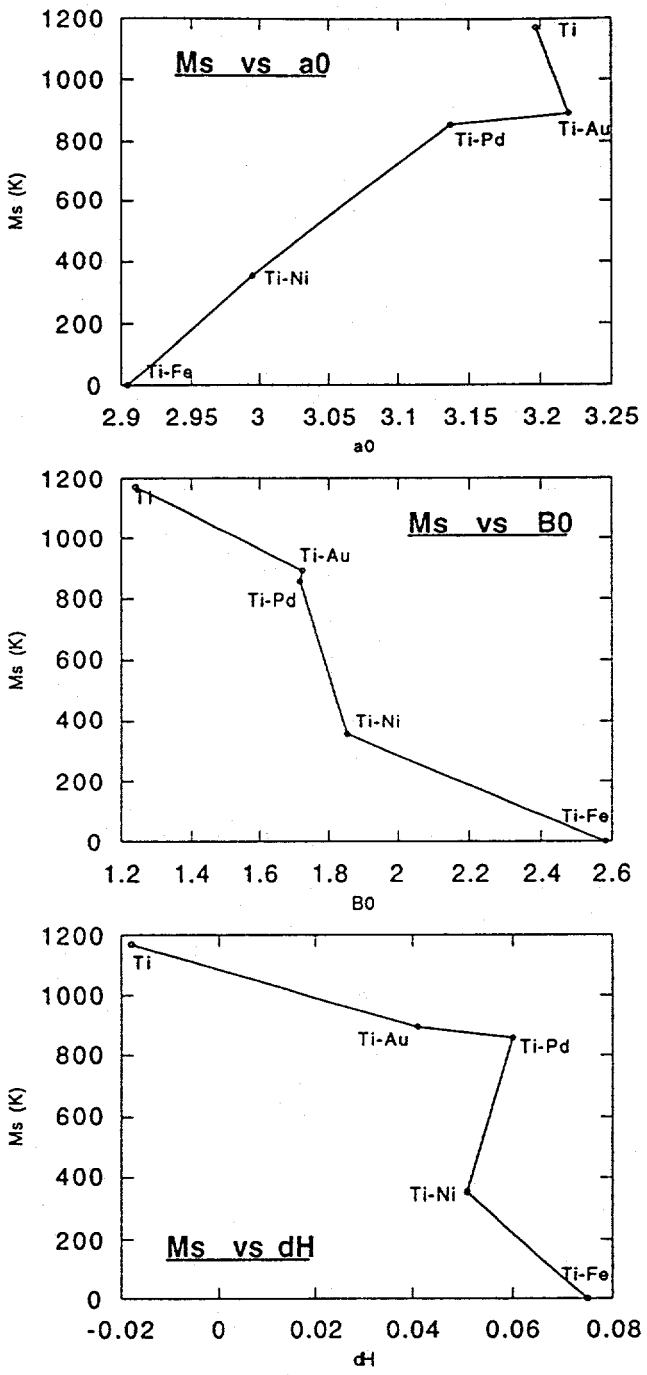

Figure 6.3: Relations of B2 phase stability and the structural properties. (a) M_s [106] vs lattice parameter; (b) M_s vs bulk modulus; (c) M_s vs heat of formation. The circles are calculated results.

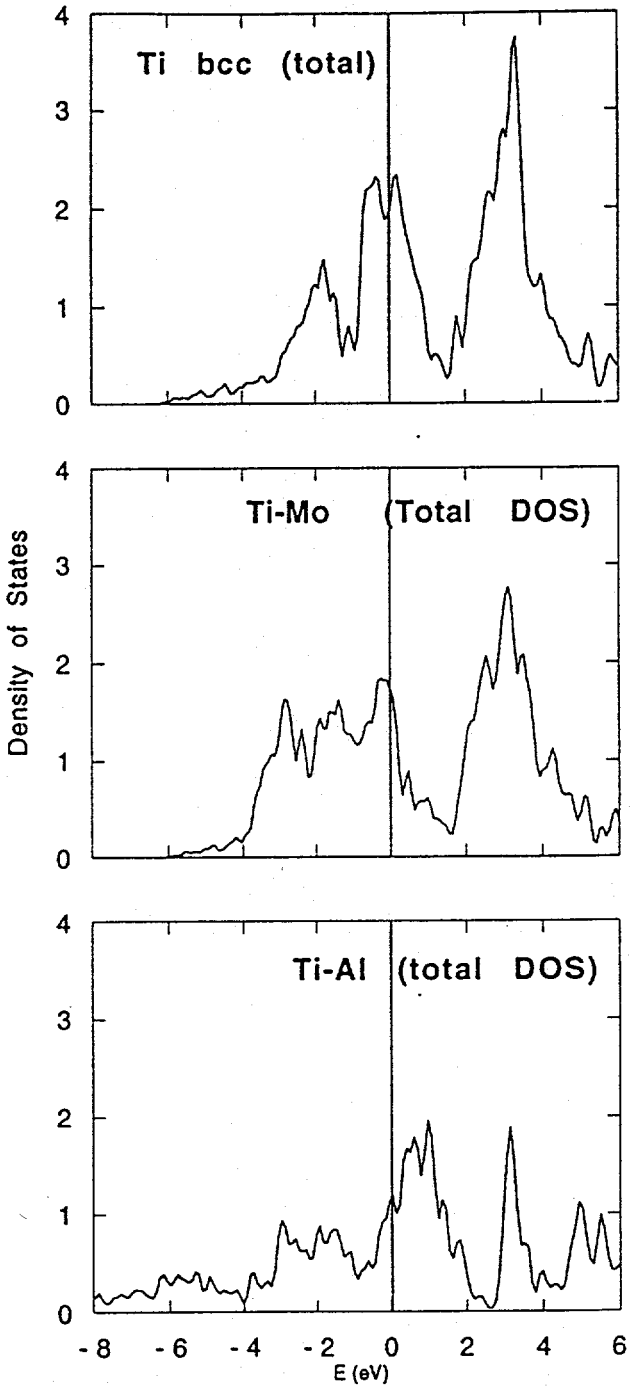

Figure 6.4: Total electronic density of states (DOS) for Ti-base alloys in B2 phase. Results for Ti (bcc), TiMo, and TiAl.

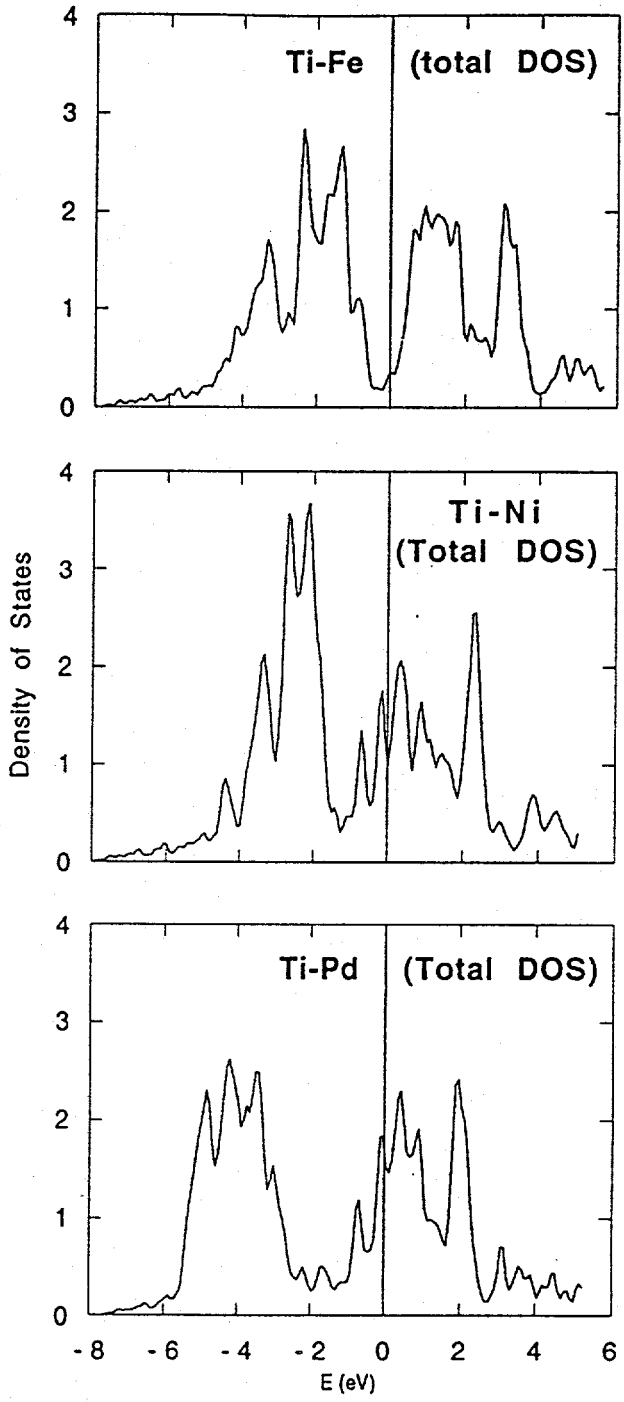

Figure 6.5: Total electronic density of states (DOS) for Ti-base alloys in B2 phase. Results for TiFe, TiNi, and TiPd.

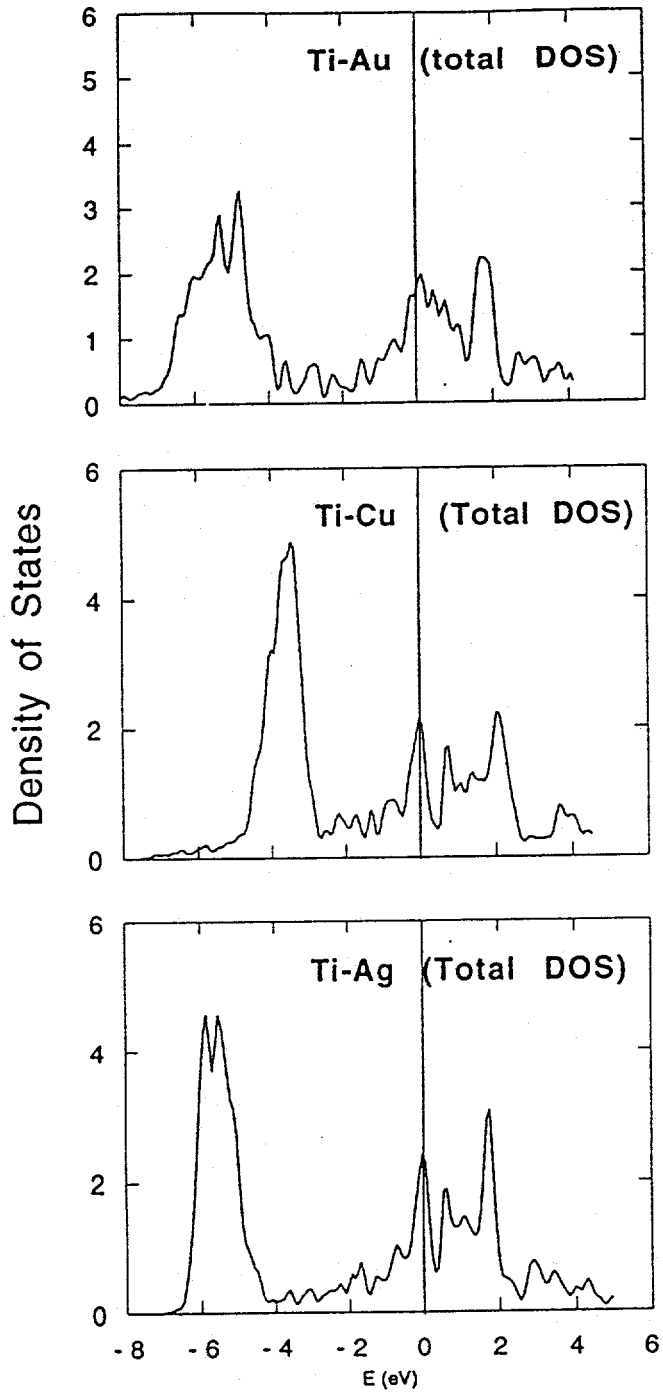

Figure 6.6: Total electronic density of states (DOS) for Ti-base alloys in B2 phase. Results for TiAu, TiCu, and TiAg.

the E_f for TiFe falls right at the minimum, in the valley between the two peaks. Ni, Pd, Au has more electrons, which moves the E_f to higher energy and higher DOS at E_f, while Mo has less electrons and that moves the E_f to lower energy and also higher DOS at E_f. Both serves to destablize the B2 structure.

Correlation is also found between M_s and the value of DOS at the Fermi level, as show in Figure 6.7. A clear trend is observed that higher M_s corresponds to higher DOS value at the Fermi level, which indicates that the Martensitic transformation is related to the electronic states around the Fermi level. We know that states around the Fermi level are mainly from the Ti d orbitals. Therefore, the above correlation suggests that we should inquire into the details of the Ti d states.

By decomposing the electronic wavefunctions into angular momentum components at the sites of the constituent elements, we calculate the Ti d state DOS, which is shown in Figures 6.8-10. We also calculate the numbers of electrons in Ti s, p, and d states by integrating inside a sphere with the Wigner-Seitz radius. The results are listed in Table 6.2. The number of Ti d electrons inside the Wigner-Seitz sphere is plotted against M_s in Figure 6.11. Except Ti of bcc structure, all other alloys fall to a descent line that increasing M_s corresponds to decreasing number of Ti D electrons.

The amount of Ti d electrons below the Fermi level decreases with decreasing B2 stability from TiFe to TiNi, TiPd, and TiAu. The more amount of Ti d states is occupied, the stronger the interbonding between the d electrons from the the two elements. These results show us the relation between the d electron bonding and the stability of the B2 structure alloys.

From the above results, we see the correlation between the electronic properties

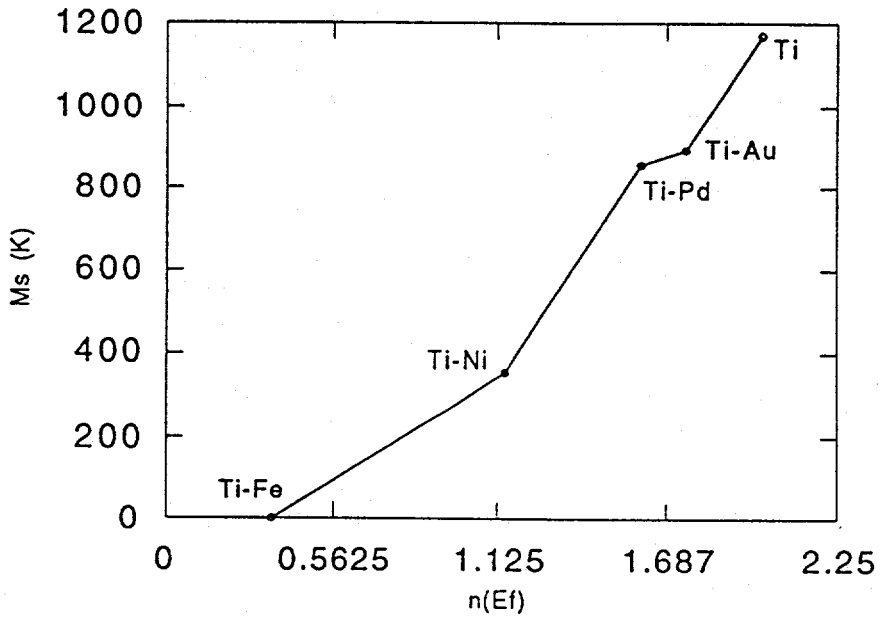

Figure 6.7: B2 stability vs total density of states at the Fermi level.

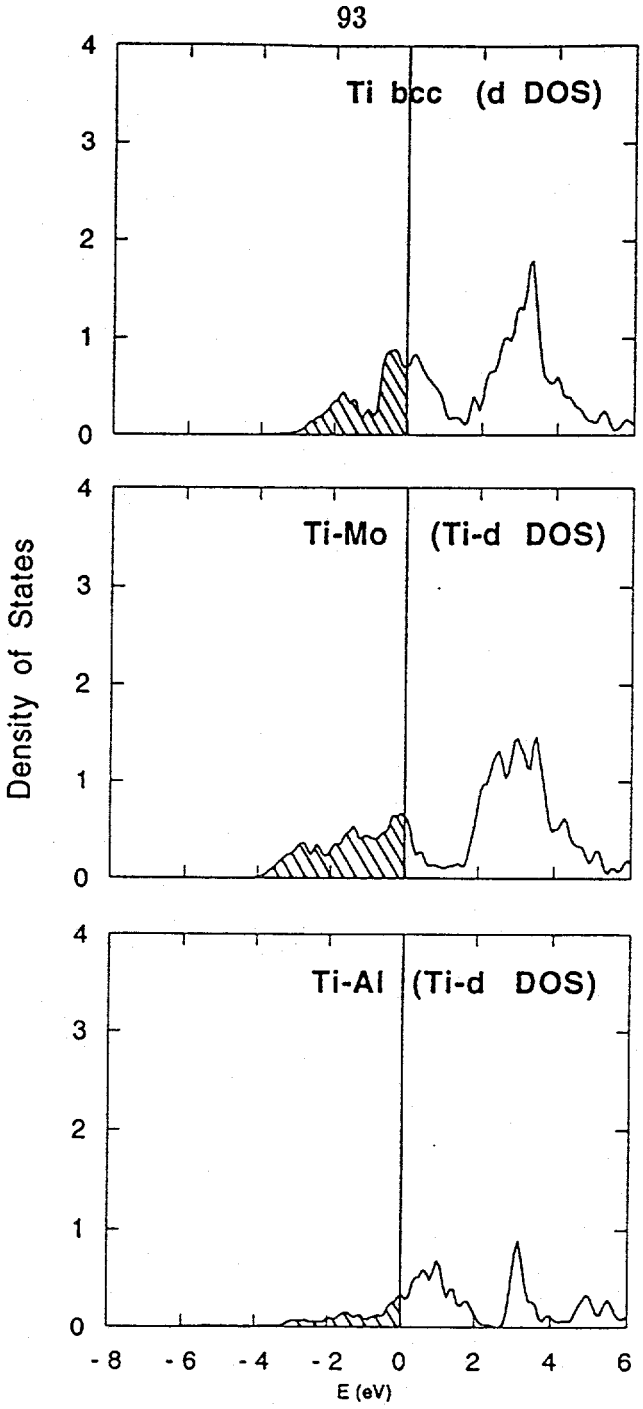

Figure 6.8: Electronic density of states (DOS) of Ti d states for Ti-base alloys in B2 phase. The shaded areas are occupied states. Results for Ti (bcc), TiMo, and TiAl.

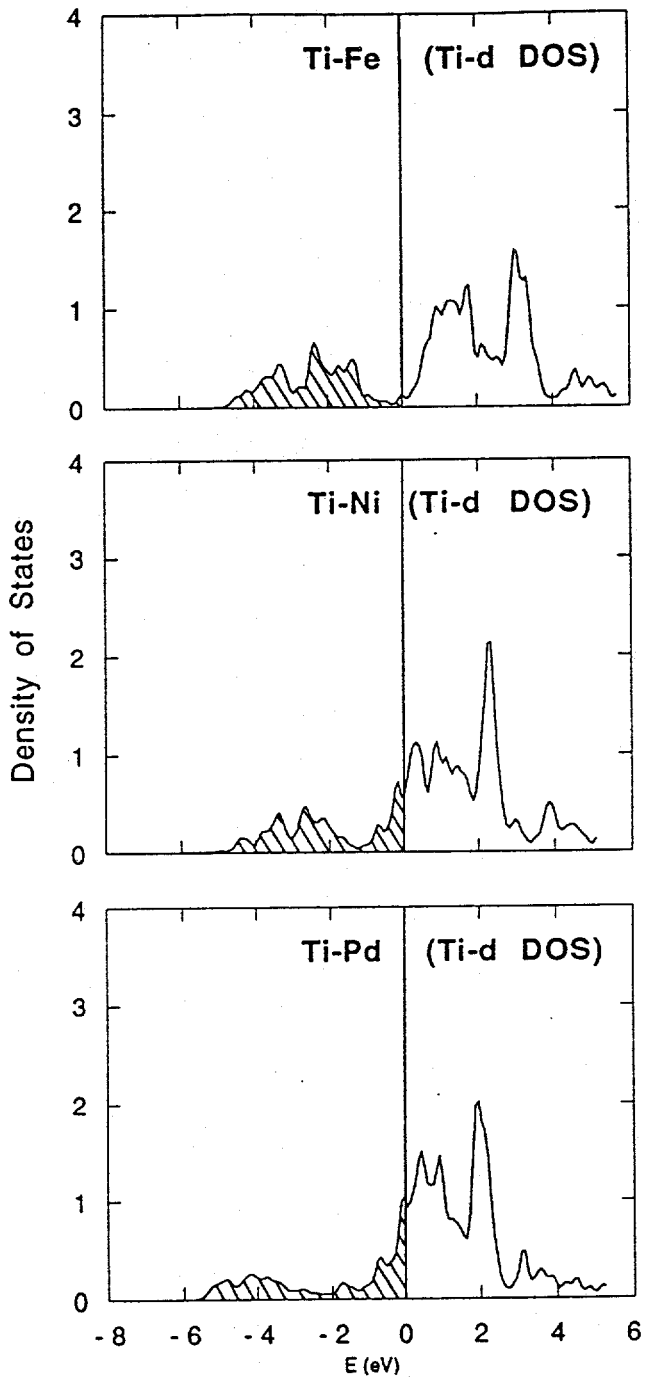

Figure 6.9: Electronic density of states (DOS) of Ti d states for Ti-base alloys in B2 phase. The shaded areas are occupied states. Results for TiFe, TiNi, and TiPd.

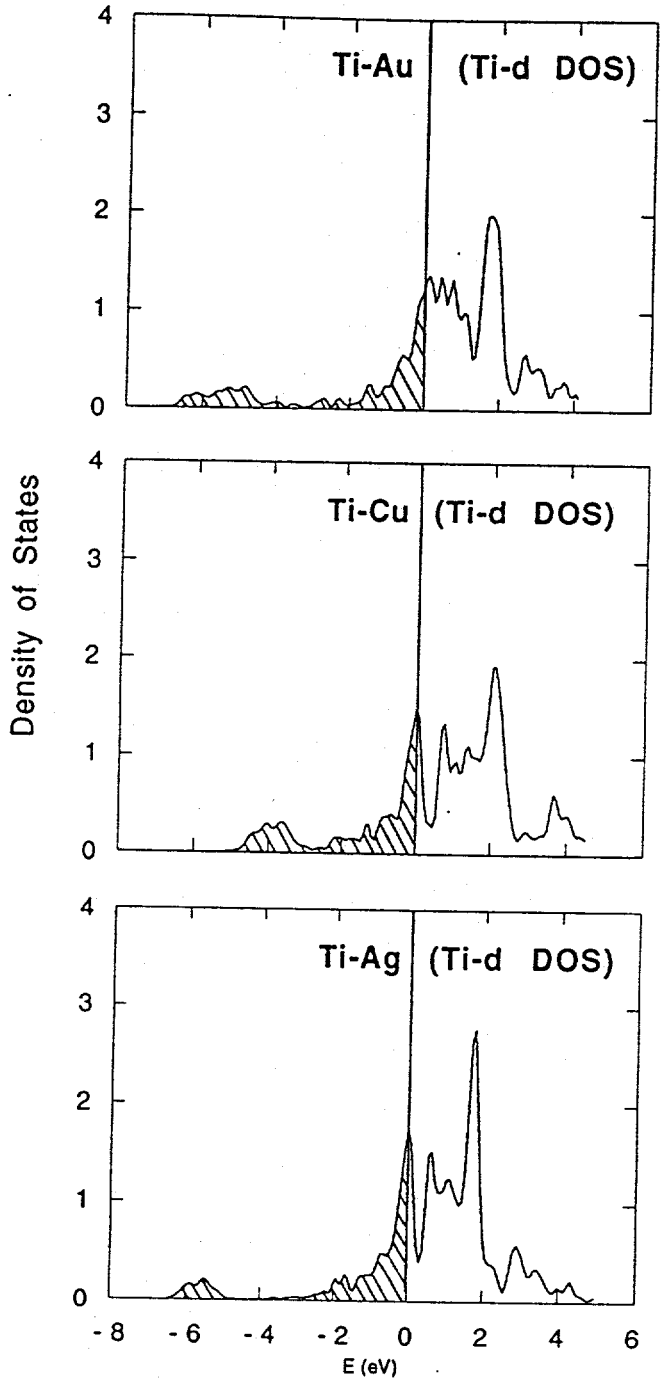

Figure 6.10: Electronic density of states (DOS) of Ti d states for Ti-base alloys in B2 phase. The shaded areas are occupied states. Results for TiAu, TiCu, and TiAg.

Table 6.2: Occupatioin numbers of Ti s, p, and d states in the alloys. Lattice constant a_0 and the Wigner-Seitz radius $r_{(WS)}$ are in Å.

Alloys	a_0	Element	$r_{(WS)}$	s	p	d	s+p+d	total
Ti(bcc)	3.197	Ti	2.98	0.648	0.632	2.660	3.940	4.021
Ti-Mo	3.137	Ti	2.98	0.666	0.749	2.751	4.165	4.353
		Mo	2.92	0.564	0.519	4.745	5.828	5.927
Ti-Fe	2.904	Ti	2.98	0.717	0.973	2.797	4.487	4.792
		Fe	2.67	0.713	0.783	6.778	2.275	2.368
Ti-Ni	2.995	Ti	2.98	0.629	0.785	2.568	3.982	4.179
		Ni	2.56	0.725	0.630	8.538	3.893	9.932
Ti-Pd	3.137	Ti	2.98	0.590	0.717	2.474	3.782	3.991
		Pd	2.87	0.771	0.687	8.697	4.156	4.234
Ti-Au	3.229	Ti	2.98	0.522	0.681	2.467	3.671	3.854
		Au	3.03	1.089	0.940	9.228	5.258	5.364
Ti-Ag	3.260	Ti	2.98	0.526	0.585	2.382	3.493	3.602
		Ag	3.04	0.856	0.868	9.591	5.315	5.393
Ti-Cu	3.068	Ti	2.98	0.581	0.679	2.510	3.770	3.902
		Cu	2.67	0.804	0.755	9.475	5.033	5.073

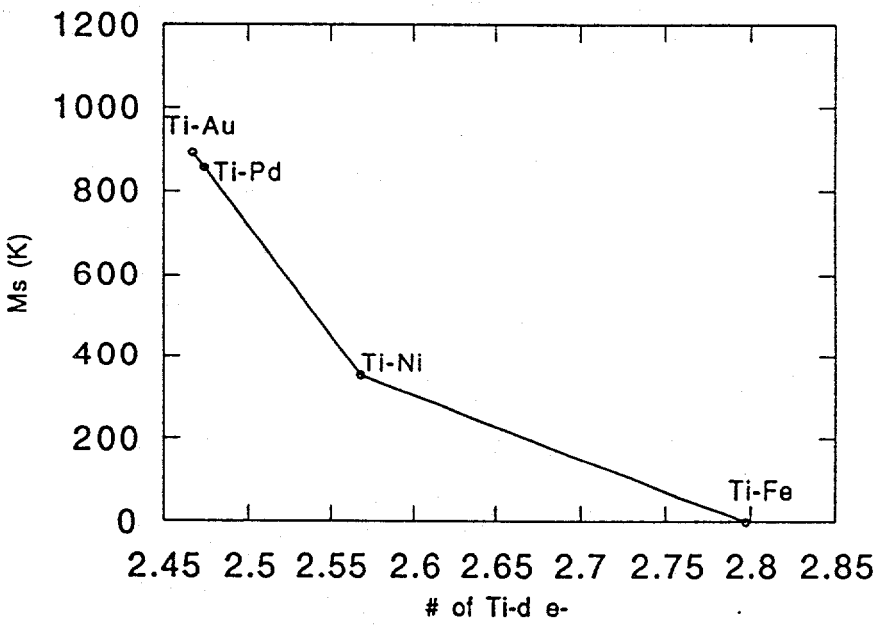

Figure 6.11: B2 stability vs Ti d state occupation number.

and the B2 structure stability of the Ti based alloys.

Summary

We performed first principles calculations to study the electronic and structural properties of a series of Ti-based binary alloys TiFe, TiNi, TiPd, TiMo and TiAu in the B2 structure. Calculations are also done for Ti in bcc structure and hypothetical B2-structured TiAl, TiAg and TiCu. Our results show corelation between the Martensitic transformation temperature (M_s) of these alloys and the electronic properties such as the total electronic density of states at the Fermi level, occupation of the Ti d states, and the degree of localization of the d states of the second element in the alloys. Angular momentum decomposition of the electronic states indicates that the bonding of Ti and the second element d electrons plays an important role in the stability of the binary alloys. Correlations between M_s and optimized structural parameters such as lattice constants and bulk moduli are also found.

BIBLIOGRAPHY

[1] For an early review, see G. LeLay, Surf. Sci. **132**, 169 (1983).

[2] K. Spiegel, Surf. Sci. **7**, 125 (1967).

[3] M. Saitoh, F. Shoji, K. Oura, and T. Hanawa, Surf. Sci. **112**, 306 (1981).

[4] M. Aono, R. Souda, C. Oshima, and Y. Ishizawa, Surf. Sci. **168**, 713 (1986).

[5] T.L. Porter, C.S. Chang, and I.S.T. Tsong, Phys. Rev. Lett. **60**, 1739(1988).

[6] R.S. Williams, R.S. Daley, J.H. Huang, and R.M. Charatan, Appl. Surf. Sci. **41/42**, 70 (1989).

[7] M. Copel and R.M. Tromp, Phys. Rev. B **39**, 12688 (1989).

[8] R.S. Daley, R.M. Charatan, and R.S. Williams, Surf. Sci. **240**, 136, (1990).

[9] K. Sumitomo, K. Tanaka, Y. Izawa, I. Katayama, F. Shoji, K. Oura, and T. Hanawa, Appl. Surf. Sci. **41/42**, 112 (1989).

[10] K. Oura, M. Watamori, F. Shoji, and T. Hanawa, Phys. Rev. B **38**, 10146(1988).

[11] K. Oura, M. Watamori, F. Shoji, and T. Hanawa, Surf. Sci. Lett. **254**, L460, (1991).

[12] M. Katayama, R.S. Williams, M. Kato, E. Nomura, and M. Aono, Phys. Rev. Lett. **66**, 2762 (1991).

[13] M. Watamori, F. Shoji, T. Hanawa, and K. Oura, Surf. Sci. **226**, 77 (1990).

[14] F. Wehking, H. Beckermann, and R. Niedermayer, Serf. Sci. **71**, 364 (1978).

[15] Y.Terada, T. Yoshizuka, K. Oura, and T. Hanawa, Surf. Sci. **114**, 65 (1982).

[16] W.C. Fan, A. Ignatiev, H. Huang, and S.Y. Tong, Phys. Rev. Lett. **62**, 1516 (1989).

[17] Y. Horio and A. Ichimiya, Surf. Sci. **133**, 393 (1983).

[18] S. Hasegawa, H. Daimon, and S. Ino, Surf. Sci. **186**, 138 (1987).

[19] A. Ichimiya, S. kohmoto, T. Fujii, and Y. Horio, Appl. Surf. Sci. **41/42**, 82 (1989).

[20] T. Takahashi, S. Nakatani, N. Okamoto, T. Ishikawa, and S. Kikuta, Jpn. J. Appl. Phys. **27**, L753 (1988).

[21] T. Takahashi, S. Nakatani, N. Okamoto, T. Ishikawa, and S. Kikuta, Surf. Sci. **242**, 54, (1991).

[22] T. Takahashi and S. Nakatani, Surf. Sci. **282**, 17 (1993).

[23] E. Vlieg, A. W. Denier van der Gon, J.F. van der Veen, J.E. MacDonald, and C. Norris, Surf. Sci. **209**, 100 (1989).

[24] E. Vlieg, E. Fontes, and J.K. Patel, Phys. Rev. B **43**, 7185 (1991).

[25] E. Vlieg, private communication, 1991.

[26] G. Le Lay, A. Chauvent, M. Manneville, and R. Kern, Surf. Sci. **9**, 190, (1981).

[27] Y. Horio and A. Ichimiya, Surf. Sci. **164**, 589 (1985).

[28] G. Raynerd, M. Hardinman, and J.A. Venables, Phys. Rev. B **44**, 13803 (1991).

[29] G. Raynerd, T.N. Doust, and J.A. Venables, Surf. Sci. **261**, 251, (1992).

[30] S. Kono, K. Higashiyama, and T. Sagawa, Surf. Sci. **165**, 21 (1986).

[31] S. Kono, T. Abukawa, N. Nakamura and K. Anno, Jpn. J. Appl. Phys. **28**, L1278 (1989).

[32] E.L. Bullock, G.S. Jerman, M. Yamada, D.J. Friedman, and C.S. Fadley, Phys. Rev. B **41**, 1703 (1990).

[33] G.S. Herman, E.L. Bullock, M. Yamada, A.P. Kaduwela, D.J. Friedman, S. Thevuthasan, Y.J. Kim, T.T. Tran, C.S. Fadley, Th. Lindner, D.E. Ricken, A.W. Robinson, and A.M. Bradshaw, Surf. Sci. **284**, 23 (1993).

[34] T. Yokotsuka, S. Kono, S. Suzuki, and T. Sagawa, Surf. Sci. **127**, 35 (1983).

[35] J.M. Nicholls, F.Salvan, and B. Reihl, Phys. Rev. B **34**, 2945 (1986).

[36] S. Kono, K. Higashiyama, T. Kinoshita, T. Miyahara, H. Kato, H. Ohsawa, Y. Enta, F. Maeda, and Y. Yaegashi, Phys. Rev. Lett. **58**, 1555 (1987).

[37] L.S.O. Johansson, E. Landemark, C.J. Karlsson, and R.I.G. Uhrberg, Phys. Rev. Lett. **63**, 2092 (1989).

[38] J. Stohr and R. Jaeger, Surf. Sci. **134**, 813 (1983).

[39] E.J. van Loenen, J.E. Demuth, R.M. Tromp, and R.J. Hamers, Phys. Rev. Lett. **58**, 373 (1987).

[40] R.J. Wilson and S. Chiang, Phys. Rev. Lett. **58**, 369 (1987); Phys. Rev. Lett. **59**, 2329 (1987).

[41] K.J. Wan, X.F. Lin, and J. Nogami, Phys. Rev. B **45**, 9509 (1992).

[42] A. Shibata, Y. Kimura, and K. Takayanagi, Surf. Sci. Lett. **275**, L697 (1992)

[43] M. Hanbucken, M. Futamoto, and J.A. Venables, Surf. Sci. **147**, 433 (1984).

[44] Y. Tanishiro, K. Takayanagi, and K. Yagi, Surf. Sci. Lett. **258**, L687 (1991).

[45] K. Oura, M. Katayama, F. Shoji, and T. Hanawa, Phys. Rev. Lett. **55**, 1486 (1985).

[46] J.H. Huang and R.S. Williams, Phys. Rev. B **38**, 4022 (1988); Surf. Sci. **204**, 445 (1988).

[47] M. Chester and T. Gustafsson, Phys. Rev. B42, 9233 (1990); Surf. Sci. **256**, 135 (1991).

[48] F. Salvan, H. Fuchs, A. Baratoff, and G. Binnig, Surf. Sci. **162**, 634 (1985).

[49] Ph. Dumas, A. Humber, G. Mathieu, P. Mathiez, C. Mouttet, R. Rolland, F. Salvan, and F. Thibaudau J. Vac. Sci. Technol. A **6**, 517 (1988).

[50] T. Hasegawa, K. Takata, S. Hosaka, and S. Hosoki J. Vac. Sci. Technol. A **8**, 241 (1990).

[51] J. Nogami, A.A. Baski, and C.F. Quate, Phys. Rev. Lett. **65**, 1611 (1990).

[52] A. Shibata, Y. Kimura, and K. Takayanagi, Surf. Sci. Lett. **273**, L430 (1992).

[53] D. Dornisch, W. Moritz, and H. Schulz, R. Feidenhans'l, M. Nielsen, F. Grey, and R.L. Johnson, Phys. Rev. B **44**, 11221 (1991).

[54] G. LeLay, and J.P. Faurie, Surf. Sci. **69**, 295 (1977).

[55] C.J. Karlsson, E. Landemark, L.S.O. Johansson, and R.I.G. Uhrberg, Phys. Rev. B **42**, 9546 (1990).

[56] J. Quinn, F. Jona, and P.M. Marcus, Phys. Rev. B **46**, 7288, (1992).

[57] K. Higashiyama, S. Kono, and T. Sagawa, Jap. J. Appl. Phys. **25**, L117 (1986).

[58] M. Ichikawa, T. Doi, and K. Hayakawa, Surf. Sci. **159**, 133 (1985).

[59] T. Ichinokawa, Y. Ishikawa, M. Kemmochi, N. Ikeda, Y. Hosokawa and J. Kirschner Surf. Sci. **176**, 397 (1986).

[60] W. Swiech, E. Bauer and M. Mundschau, Surf. Sci. **253**, 283 (1991).

[61] N. Osakabe, Y. Tanishiro, K. Yagi and G. Honjo, Surf. Sci. **97**, 393 (1980).

[62] S.Y. Tong and H. Huang, Surf. Sci. Lett., **243**, L46, (1991).

[63] S.H. Chou, A.J. Freeman, S. Grigoras, T.M. Gentle, B. Delley, and E. Wimmer, J. Chem. Phys. **89**, 5177 (1988).

[64] Q.Q. Zheng and Z. Zeng, Surf. Sci. **195**, L173 (1988).

[65] A. Fortunelli, O. Salvetti, and G. Villani, Surf. Sci., **244**, 355, (1991).

[66] C.T. Chan and K.M. Ho, Surf. Sci. **217**, 403 (1989).

[67] Y.G. Ding, C.T. Chan, and K.M. Ho, Phys. Rev. Lett., **67**, 1454 (1991).

[68] S. Watanabe, M. Aono, and M. Tsukada, Phys. Rev. B **44**, 8330, (1991).

[69] Y.G. Ding, C.T. Chan, and K.M. Ho, Surf. Sci. Lett. **275**, L691 (1992).

[70] M.L. Cohen and V. Heine, Solid State Physics, **24**, 37 (1970).

[71] J.P. Walter and M.L. Cohen, Phys. Rev. Lett. **26**, 17 (1971); M.L. Cohen, Science **179**,1189 (1973).

[72] J.A. Appelbaum and D.R. Hamann, Rev. Mod. Phys. **48**, 3 (1976).

[73] M. Schlüter, J.R. Chelikowsky, S.G. Louie, and M.L. Cohen, Phys. Rev. B **12**, 4200 (1975).

[74] M.L. Cohen, M. Schlüter, J.R. Chelikowsky, and S.G. Louie, Phys. Rev. B **12**, 4475 (1975).

[75] T. Starkloff and J.D. Joannopoulos, Phy. Rev. B **16**, 5212 (1977).

[76] A. Zunger and M.L. Cohen, Phys. Rev. B **18**, 5449 (1978).

[77] D.H. Hamman, M. Schluter and C. Chiang, Phys. Rev. Lett. **43**, 1494 (1979).

[78] G. Kerker, J. Phys. C **13**, L189 (1980).

[79] M.T. Yin and M.L. Cohen, Phys. Rev. B **25**, 7403 (1982).

[80] S.G. Louie, S. Froye, and M.L. Cohen, Phys. Rev. B **26**, 1738, (1982).

[81] J. Ihm, A. Zunger, and M.L. Cohen, J. Phys. C **12**, 4401 (1979).

[82] M.L. Cohen, Physica Scripta T **1**, 5 (1982).

[83] J. Ihm and M.L. Cohen, Solid State Comm. **29**, 711 (1979).

[84] J. Ihm, D.J. Chadi, M.L. Cohen, Phy. Rev. B **21**, 4592 (1980).

[85] M.T. Yin, M.L. Cohen, Phys. Rev. B **24**, 2303 (1981).

[86] J. E. Northrup, J. Ihm, and M. L. Cohen, Phys. Rev. Lett, **47**, 1910 (1981).

[87] J. E. Northrup and M. L. Cohen, Phys. Rev. Lett. **49**, 1349 (1982).

[88] J. A. Applebaum and D. R. Hamann, Phys. Rev. B **6** 2166 (1972).

[89] J. A. Applebaum and D. R. Hamann, Phys. Rev. Lett. **31** 106 (1973).

[90] J. A. Applebaum and D. R. Hamann, Phys. Rev. Lett. **32** 225 (1974).

[91] J. R. Chelikowsky, Phys. Rev. B **15** 3236 (1977).

[92] J. Ihm, S. G. Louie and M. L. Cohen, Phys. Rev. B **17** 769 (1978).

[93] D. Vanderbilt and S. G. Louie, Phys. Rev. B **30** 6118 (1984).

[94] S. G. Louie K. M. Ho, J. R. Chelikowsky, and M. L. Cohen, Phys. Rev. Lett. **40** 1593 (1976).

[95] S. G. Louie K. M. Ho, J. R. Chelikowsky, and M. L. Cohen, Phys. Rev. B **25** 5627 (1977).

[96] S. G. Louie, Phys. Rev. Lett. **40** 1525 (1978).

[97] G. P. Kerker, K. M. Ho, and M. L. Cohen, Phys. Rev. Lett. **40** 1593 (1978).

[98] G. P. Kerker, K. M. Ho, and M. L. Cohen, Phys. Rev. B **18** 5473 (1978).

[99] C. T. Chan and S. G. Louie, Phys. Rev. B **33** 2861 (1986).

[100] K. M. Ho, and K. P. Bohnen, Phys. Rev. Lett. **59**, 1833 (1987).

[101] N.Takeuchi, C. T. Chan, and K. M. Ho. Phys. Rev. Lett. **63**, 1273 (1989).

[102] P. Hohenberg and W. Kohn, Phys. Rev. **136**, B864 (1964); W. Kohn and L. J. Sham, Phys. Rev. **140**, A1133 (1965).

[103] J. Ihm, M.T. Yin, and M.L. Cohen, solid State Comm. **37**, 491 (1981).

[104] K. M. Ho, J. Ihm, and J. D. Joannopoulos, Phys. Rev. B **25**, 4260 (1982).

[105] H. Hellman, *Einführung in die Quantenchemie* (Deuticke, Leipzig, 1937); R. P. Feynman, Phys. Rev. **56** 340 (1939).

[106] S.A. Shabalovskaja, Phys. Status Solidi b **132**, 327(1985).

[107] F.E. Wang, B.F. DeSavage, W.J. Buehler, and W.R. Hosler, J. Appl. Phys. **39** 2166 (1968).

[108] For a review see for example, W. E. Pickett Comp. Phys. Rep. **9** 115 (1989).

[109] J. A. Appelbaum and D. R. Hamann, Phys. Rev. B **8**, 1777 (1973); M. Schlüter, J. R. Chelikowsky, S. G. Louie, and M. L. Cohen, Phys. Rev. B **12**, 4200 (1975).

[110] C. Herring, Phys. Rev. **57**, 1169 (1940).

[111] J. C. Phillips and L. Kleinman, Phys. Rev. **116**, 287 (1959).

[112] D. R. Hamann, M. Schlüter, and C. Chiang, Phys. Rev. Lett. **43**, 1494 (1979); G. B. Bachelet and M. Schluter, Phys. Rev. B **25**, 2103 (1982); L. Kleinman, Phys. Rev. B **21**, 2630 (1980).

[113] F. Herman and S. Skillman, in *Atomic Structure Calculation* (Prentice-Hall, Englewood Cliffs, N. J., 1963).

[114] L. Hedin and B. I. Lundqvist, J. Phys. C **4**, 2064 (1971).

[115] For a review see for example R. O. Jones and O. Gunnarsson, Rev. Mod. Phys. **61**, 689 (1989); or see, e.g., Theory of the Inhomogeneous Electron Gas, Eds. NH. March and S. Lundqvist (Plenum, New York, 1983).

[116] E. Wigner, Phys. Rev. **46**, 1002 (1934).

[117] J. Perdew and A. Zunger, Phys. Rev. B **23**, 5048 (1980); C. M. Ceperly and B. J. Alder, Phys. Rev. Lett. **45**, 566 (1980).

[118] P. P. Ewald, Ann. Phys. (Leipzig) **64**, 253 (1921); K. Fuchs, Proc. R. Soc. London, Ser. A **151**, 585 (1935).

[119] S. G. Louie, K. M. Ho, and M. L. Cohen, Phys. Rev. B **19**, 1774 (1979).

[120] N. Takeuchi, C. T. Chan, and K. M. Ho, Phys. Rev. B **40**. 1565 (1989).

[121] C. Elsässer, N. Takeuchi, K. M. Ho, C. T. Chan, P. Braun, an M. F"ahnle, J. Phys. C.M. **2** 4371 (1990).

[122] J. C. Slater, *Self-consistent Field for Molecules and Solids* (McGraw-Hill, New York, 1974).

[123] J. A. Venables, J. S. Drucker, M. Krishnamurthy, G. Raynerd, and T. Doust, Mater. Res. Soc. Symp. Proc. **198**, 93(1990).

[124] Guo-Xin Qian and D.J. Chadi, Phys. Rev. B **35**, 1288(1987).

[125] J. Tersoff and D.R. Hamann, Phys. Rev. Lett. **50**, 1998 (1983).

[126] D. Vanderbilt, Phys. Rev. B **32**, 8412 (1985).

[127] A.M. Rappe, K.M. Rabe, E. Kaxiras, and J.D. Joannopoulos, Phys. Rev. B **41**, 1227 (1990).

[128] N. Troullier and J.L. Martins, Phys. Rev. B **43**, 1993 (1991).

[129] D. Vanderbilt, Phys. Rev. B **41**, 7892 (1990).

[130] D.D. Koelling and B.N. Harmon, J. Phys. C **10**, 3107 (1977).

[131] S.G. Louie, S. Froyen, and M.L. Cohen, Phys. Rev. B **26**, 1738 (1982).

[132] K.J. Wan, X.F. Lin, and J. Nogami, preprint, (1993).

[133] H.H. Weitering, N.J. DiNardo, R. Pérez-Sandoz, J. Chen, and E.J. Mele, preprint, (1993).

[134] C. Kittel, Introduction to Solid State Physics(Wiley, New York, 1986).